Effects of Cr/Ni ratio on physical properties of Cr-Mn-Fe-Co-Ni high-entropy alloys

Wagner, Christian; Ferrari, Alberto; Schreuer, Jürgen; Couzinié, Jean Philippe; Ikeda, Yuji; Körmann, Fritz; Eggeler, Gunther; George, Easo P.; Laplanche, Guillaume

DOI
10.1016/j.actamat.2022.117693

Publication date
2022

Document Version
Final published version

Published in
Acta Materialia

Citation (APA)
Wagner, C., Ferrari, A., Schreuer, J., Couzinié, J. P., Ikeda, Y., Körmann, F., Eggeler, G., George, E. P., & Laplanche, G. (2022). Effects of Cr/Ni ratio on physical properties of Cr-Mn-Fe-Co-Ni high-entropy alloys. *Acta Materialia*, *227*, Article 117693. https://doi.org/10.1016/j.actamat.2022.117693

Acta Materialia 227 (2022) 117693

Contents lists available at ScienceDirect

Acta Materialia

journal homepage: www.elsevier.com/locate/actamat

Effects of Cr/Ni ratio on physical properties of Cr-Mn-Fe-Co-Ni high-entropy alloys

Christian Wagner[a,*], Alberto Ferrari[b], Jürgen Schreuer[c], Jean-Philippe Couzinié[d], Yuji Ikeda[e,f], Fritz Körmann[b,f], Gunther Eggeler[a], Easo P. George[g,h], Guillaume Laplanche[a]

[a] Institut für Werkstoffe, Ruhr-Universität Bochum, D-44801 Bochum, Germany
[b] Materials Science and Engineering, Delft University of Technology, 2628CD Delft, Netherlands
[c] Institut für Geologie, Mineralogie und Geophysik, Ruhr-Universität Bochum, D-44780 Bochum, Germany
[d] Université Paris Est, Institut de Chimie et des Matériaux Paris-Est (UMR7182), CNRS, UPEC, 2-8 rue Henri Dunant, F-94320, Thiais, France
[e] Institut für Materialwissenschaft, Universität Stuttgart, D-70569 Stuttgart, Germany
[f] Max-Planck-Institut für Eisenforschung GmbH, Max-Planck-Straße 1, D-40237 Düsseldorf, Germany
[g] Materials Science and Technology Division, Oak Ridge National Laboratory, Oak Ridge, Tennessee 37831-6115, USA
[h] Department of Materials Science and Engineering, University of Tennessee, Knoxville, Tennessee. 37996-2100, USA

ARTICLE INFO

Article history:
Received 15 November 2021
Revised 25 January 2022
Accepted 27 January 2022
Available online 29 January 2022

Keywords:
CoCrFeMnNi
Elastic constants
Coefficient of thermal expansion
Stacking fault energy
Curie temperature
Generalized stacking fault energy

ABSTRACT

Physical properties of ten single-phase FCC $Cr_xMn_{20}Fe_{20}Co_{20}Ni_{40-x}$ high-entropy alloys (HEAs) were investigated for $0 \leq x \leq 26$ at%. The lattice parameters of these alloys were nearly independent of composition while solidus temperatures increased linearly by ~30 K as x increased from 0 to 26 at.%. For $x \geq 10$ at.%, the alloys are not ferromagnetic between 100 and 673 K and the temperature dependencies of their coefficients of thermal expansion and elastic moduli are independent of composition. Magnetic transitions and associated magnetostriction were detected below ~200 K and ~440 K in $Cr_5Mn_{20}Fe_{20}Co_{20}Ni_{35}$ and $Mn_{20}Fe_{20}Co_{20}Ni_{40}$, respectively. These composition and temperature dependencies could be qualitatively reproduced by *ab initio* simulations that took into account a ferrimagnetic ↔ paramagnetic transition. Transmission electron microscopy revealed that plastic deformation occurs initially by the glide of perfect dislocations dissociated into Shockley partials on {111} planes. From their separations, the stacking fault energy (SFE) was determined, which decreases linearly from 69 to 23 $mJ \cdot m^{-2}$ as x increases from 14 to 26 at.%. *Ab initio* simulations were performed to calculate stable and unstable SFEs and estimate the partial separation distances using the Peierls-Nabarro model. While the compositional trends were reasonably well reproduced, the calculated intrinsic SFEs were systematically lower than the experimental ones. Our *ab initio* simulations show that, individually, atomic relaxations, finite temperatures, and magnetism strongly increase the intrinsic SFE. If these factors can be simultaneously included in future computations, calculated SFEs will likely better match experimentally determined SFEs.

1. Introduction

The equiatomic face-centered cubic (FCC) CrMnFeCoNi alloy, the so-called Cantor alloy [1], is a model high-entropy alloy (HEA) that has received considerable interest in, *e.g.*, materials science and engineering [2–5], diffusion [6,7], corrosion/oxidation [8–11], and electrocatalysis [12]. Due to its good malleability [13–15], which made it the pioneering HEA to be thermomechanically processed and investigated in bulk form, and interesting mechanical properties at cryogenic temperatures, *e.g.*, excellent tensile properties [13,14], outstanding fracture toughness [2], high resistance to low-cycle-fatigue [16–18] and fatigue crack propagation [19,20], it is one of the most studied HEAs of the last decade. The outstanding damage tolerance of the CrMnFeCoNi HEA is thought to result from its relatively low intrinsic stacking fault energy ($\gamma_{isf} \approx 30$ mJ/m^2, [21,22]) which promotes planar glide of dissociated dislocations [5,14], delays the onset of cross-slip [5], and induces mechanical twinning [14,23], thereby resulting in sustained, high work hardening rate.

* Corresponding author.
E-mail addresses: christian.wagner-g5n@ruhr-uni-bochum.de (C. Wagner), a.ferrari-1@tudelft.nl (A. Ferrari).

https://doi.org/10.1016/j.actamat.2022.117693

Several studies have investigated the effects of increased Cr concentration on phase stability and mechanical properties in non-equiatomic CrMnFeCoNi HEAs [24–28]. Zaddach *et al.* [24,25] were the first to vary the Cr/Ni ratio of the equiatomic CrMnFeCoNi alloy. Using an X-ray diffraction-based method they showed that, compared to the equiatomic alloy, the stacking fault energy (SFE) of the non-equiatomic $Cr_{26}Mn_{20}Fe_{20}Co_{20}Ni_{14}$ HEA is lower by a factor of ~5. Even though SFE can be estimated relatively easily from XRD data, this method is known to be less accurate than SFE derived from direct measurements of Shockley partial separations by TEM. Additionally, since the XRD technique requires knowledge of single-crystal elastic moduli[1], which were not experimentally available at that time, Zaddach *et al.* [24] computed the elastic stiffness coefficients by density functional theory (DFT), which added a certain degree of uncertainty to the determined SFEs. Furthermore, the authors investigated as-cast alloys (prone to dendritic solidification) and mechanically alloyed powders (typically contaminated by steel balls) produced from raw materials with rather low purities (99 wt.%). As the real composition and homogeneity of their specimens were not reported, it is unclear the extent to which they may have affected the SFEs reported by Zaddach *et al.* [24]. One of the objectives of the present work is to carefully evaluate the SFEs of this prominent class of HEAs by investigating chemically homogeneous alloys of known composition using state of the art TEM experiments.

Earlier attempts to produce the $Cr_{26}Mn_{20}Fe_{20}Co_{20}Ni_{14}$ HEA (lowest SFE) in bulk form with a recrystallized microstructure showed that a high Cr/Ni ratio promotes the formation of the topologically close-packed σ phase [25,29]. Associated with this precipitation was a loss of ductility [25,26] due to the brittle nature of this σ phase [30]. Recently, the phase stability of the $Cr_{26}Mn_{20}Fe_{20}Co_{20}Ni_{14}$ HEA was investigated in detail by Laplanche *et al.* [31,32] who proposed a pseudo-binary phase diagram for CrMnFeCoNi HEAs with different Cr/Ni ratios. More importantly, the Cr/Ni-dependent solvus temperature of the σ phase was established that can guide the design and heat treatment of a series of single-phase FCC CrMnFeCoNi HEAs with high Cr/Ni ratios and extremely low SFEs.

Based on this knowledge, the present work aims to: (1) process chemically homogeneous, single-phase FCC CrMnFeCoNi HEAs with different Cr/Ni ratios and recrystallized microstructures; (2) experimentally assess composition-dependent physical properties of these alloys including their dilatation behavior, elastic and magnetic properties, and SFEs; (3) investigate how the precipitation of the σ phase affects the SFE, and (4) theoretically simulate these properties and compare with experimental data.

2. Experimental methods

2.1. Material processing

Ten $Cr_xMn_{20}Fe_{20}Co_{20}Ni_{40-x}$ alloys (x = 0, 5, 10, 14, 16, 18, 20, 22, 24, and 26 at. %) were produced starting from pure elements (purity > 99.9 wt.%). Mn and Co were acid cleaned to remove their oxide layers, as described in Refs. [33,34]. Cr, Fe, and Ni had no apparent surface oxide and were therefore not etched with acid. Alloy ingots (45 mm in diameter) were produced from the raw metals by vacuum induction melting and casting as described elsewhere [35]. The cast ingots were machined down to a diameter of 40 mm and then homogenized at 1473 K for 48 h in evacuated fused silica tubes. Subsequently, the ingots were swaged at room temperature (RT) to a final diameter of 16.5 mm as described in Ref. [35]. Finally, the swaged rods were recrystallized in air at temperatures between 1173 K and 1373 K for times ranging from 5 min to 1 h followed by air cooling.

2.2. Microstructure, phase analysis, texture, and chemical composition

After recrystallization, metallographic samples were extracted from each alloy with surfaces parallel to the longitudinal axis of the rods. They were ground with SiC papers to a grit size of 8 µm and polished with progressively finer diamond suspensions (6 to 1 μm). Final polishing occurred in a "Buehler Vibromet 2″ for 48 h under a 200 g load and immersed in a mixture of 300 ml of distilled water and 150 ml "MasterMetTM Colloidal Silica Polishing Suspension" with a particle size of 0.06 μm.

An X-ray diffractometer of type PANalytical X'Pert Pro MRD equipped with a 4-bounce germanium (220) monochromator (CuKα radiation λ = 0.154 nm) was used for phase characterization. The XRD patterns were recorded using the following parameters: 2θ-range from 20° to 120°, step size $\Delta 2\theta$ = 0.006° and an integration time of 280 s.

Chemical analyses were performed using a Zeiss scanning electron microscope (SEM) of type Leo 1530 VP equipped with an EDX detector. Texture analysis and grain size measurements were carried out by electron backscatter diffraction (EBSD) and backscatter electron imaging (BSE), respectively, in a Quanta FEI 650 ESEM equipped with a Hikari XP camera (EDAX, AMETEK). EBSD was carried out using an accelerating voltage of 30 kV, a working distance of 11–15 mm, and step sizes between 1 and 4 µm, depending on grain size. Kikuchi patterns were indexed with TSL OIM Analysis software (version 6.2.0). Inverse pole figures (IPFs) were chosen to represent the texture parallel to the rod axis since no texture was found in a direction perpendicular to the swaging direction. These IPFs were calculated using the harmonic expansion method up to a series expansion degree of 22 and a Gaussian half-width of 5°.

Average grain sizes were determined following ASTM E-112 [36] using four parallel horizontal and vertical lines per micrograph. Four BSE micrographs with at least 1000 intercepts per micrograph were evaluated, resulting in at least 4000 intercepts for each material state. From these measurements, mean grain size (D), defined here as the mean intercept distance (excluding twin boundaries), and standard deviation were obtained.

2.3. Thermal expansion coefficient and elastic moduli

Cylindrical samples (10 mm length × 4 mm diameter) were electric discharge machined (EDM) from recrystallized rods with longitudinal axes parallel to the rod axis and their thermal expansion measured between 100 K and 673 K at a heating rate of 2 K/min in helium purge gas using a Netzsch inductive gauge dilatometer of type "DIL 402 C". The dilatometer was calibrated using standard fused-silica samples. Each run was repeated at least twice to check for reproducibility.

The elastic behavior of the alloys was studied using resonant ultrasound spectroscopy (RUS), which is based on the mechanical resonance frequencies of a freely vibrating body [37]. Cuboid specimens with dimensions of about 10 × 7 × 5 mm^3 were cut from the recrystallized rods by EDM and their densities first measured at RT using the buoyancy method in pure water. The RUS set-up consisted of a network analyzer of type FRA5087 and a BA4825 signal amplifier (both from NF Corporation) for signal generation and detection, a cascading temperature controller Eurotherm 2704, and a commercial Netzsch resistance furnace in combination with a liquid nitrogen supply and thermocouples of type E. To approximate the boundary condition of free vibration, the sample was weakly clamped at opposite corners between two corundum rods connected to piezoelectric transducers. At the sample, temperature

[1] Keynote lecture by Prof. Carl Koch "Nanostructured High Entropy Alloys: A Review" at the TMS2021 virtual meeting.

stability was better than ±0.1 K with an uncertainty of about ±2 K. In the frequency range from 100 to 800 kHz, resonance spectra were recorded between 100 K and 673 K in steps of 10 K, while the furnace was continuously flushed with helium. Using the shape, dimensions, and density of the sample, its aggregate elastic stiffnesses c_{11}, c_{12}, and $c_{44} = (c_{11} - c_{12})/2$ were determined assuming isotropic elasticity and using a non-linear least-squares procedure involving 60 resonances at each temperature. As will be shown later, the assumption of an elastically isotropic medium is justified because the alloys investigated have homogeneous compositions, small average grain size, and nearly random orientation of grains.

For two alloy compositions, strong ultrasound attenuation was observed in a certain temperature range. Therefore, the inverse quality factors Q^{-1} of selected resonances were calculated by approximating their profiles with modified Lorentzian functions

$$A_i(f) = A_{0i}\left(1 + \frac{(f - f_i)^2}{0.25\ w_i^2}\right)^{n_i}, \quad (1)$$

where A_{0i} and f_i are amplitude and frequency, respectively, of the i^{th} mode, the exponent $n_i < 0$ describes the shape of the resonance peak and the parameter w_i can be interpreted as full-width at half-maximum, which is related to the inverse quality factor of the resonance by $Q^{-1} = w_i/f_i$.

From the stiffness coefficients, Young's modulus (E) and shear modulus (G) were calculated using standard relations [38], which are provided in supplementary materials, see Eqs. S1 and S2. The temperature dependencies of E and G were fitted to the empirical equation proposed by Varshni [39], from which the temperature dependence of Poisson's ratio ν was obtained assuming isotropic elasticity, see Eqs. S3-S5. It is worth noting that even small uncertainties of about ±3% in E and G, lead to a comparatively large uncertainty of about ±20% in ν due to the error propagation.

2.4. Curie temperature

As the $Mn_{20}Fe_{20}Co_{20}Ni_{40}$ alloy was found to be magnetic at RT, its Curie temperature was determined using a TGA 2050 CE thermobalance (TA Instruments GmbH) using the same procedure as reported in Ref. [40]. Briefly, a permanent magnet was placed below the thermobalance to apply a downward magnetic force on the specimen and the apparent weight of the specimen recorded continuously as a function of temperature. A sudden decrease of the apparent specimen weight occurred when the alloy became non-magnetic, which was noted as the Curie temperature.

2.5. Determination of the solidus and liquidus temperatures

The solidus and liquidus temperatures of the alloys were determined using a high-temperature differential scanning calorimeter (DSC) of type "HDSC PT1600" (Linseis Messgeräte GmbH). Prior to a measurement, the chamber was filled with Ar and evacuated three times to a pressure of $9 \cdot 10^{-3}$ mbar. Samples from each alloy weighing ~0.1 g were then heated to 1860 K at 5 K/min under flowing Ar (4 l/h). From the heating curve, the solidus and liquidus temperatures were determined using a tangent method. For more details, the reader may refer to Ref. [41]. Each measurement was repeated three times from which mean values and deviations were calculated.

2.6. Investigations using transmission electron microscopy

Prior to transmission electron microscopy (TEM) investigations, dislocations were introduced into the recrystallized alloys by compressing cylindrical specimens (length 10 mm, diameter 4 mm) at 293 K to ~4% plastic strain at an engineering strain rate of 10^{-3} s^{-1}. Slices were then cut at 45° to the loading axis, ground to a thickness of ~100 µm using 600-grit SiC paper, and discs with a diameter of 3 mm were punched out of the slices. The discs were double-jet electrochemically thinned in a Struers TenuPol-5 at 16 V, with a pump flow rate of 30 (no units are provided by Struers) at 253 K using an electrolyte consisting of 70 vol. % methanol, 20 vol. % glycerin and 10 vol. % perchloric acid.

To determine the Burgers vectors of the dislocations, $\boldsymbol{g} \cdot \boldsymbol{b}$ analysis was carried out in a Tecnai Supertwin F20 G2 operating at 200 kV, where $\boldsymbol{g}$ is the diffraction vector and $\boldsymbol{b}$ the Burgers vector. From the separation distance (d) between Shockley partials on {111} planes, and assuming isotropic elasticity, the intrinsic stacking fault energy (γ_{isf}) was calculated as described in [42] knowing the elastic constants (G, ν) and the angle (β) between the dislocation line and the Burgers vector of the perfect dislocation, see Eq. S10. To facilitate measurement of d and $\boldsymbol{g} \cdot \boldsymbol{b}$ analysis, TEM foils were cut at 45° to the loading axis (maximum shear stress), and a grain with a {111} plane lying nearly parallel to the plane of the TEM foil (*i.e.*, with a <111> zone-axis) was selected. Weak-beam dark-field (WBDF) imaging was employed using the $\boldsymbol{g}(3\boldsymbol{g})$-diffraction condition recommended by Cockayne *et al.* [43]. From WBDF images, the separation distance between Shockley partials (d_{obs}) was measured at three points along straight segments of isolated dislocations. An average value from each set of three measurements and the associated deviation from the mean value (taken here as the error bar) was obtained for dislocations with varying screw/edge characters.

From the d_{obs} values, the actual separations between Shockley partials (d) was obtained using the corrections and procedures recommended in [44,45], see Eqs. S6-S9. To improve WBDF image resolution and facilitate observation of the very closely spaced partials in the alloy with the highest SFE, a $\boldsymbol{g}(4\boldsymbol{g})$-diffraction condition was used [46]; however, it could be applied in only very thin parts of the TEM foil because of the strong decrease in the effective extinction distance [47]. The other alloys with lower SFEs could be successfully analyzed using $\boldsymbol{g}(3\boldsymbol{g})$.

3. Computational details

First-principles calculations were employed to study the effect of the Cr/Ni ratio on magnetic properties and the γ-surface (also called generalized stacking fault energy (GSFE) surface [48]). Electronic structure calculations were performed within the density functional theory (DFT) framework with the exact-muffin-tin-orbital (EMTO) method [49–53] in combination with the full-charge-density method [54,55], and with the projector-augmented wave (PAW) method [56,57] implemented in VASP 5.4 [58–60]. Electronic densities and total energies were calculated within the generalized gradient approximation of the Perdew-Burke-Ernzerhof form [61]. Brillouin zones were sampled by meshes with more than 10 000 k-points per reciprocal atom. For EMTO, ideal mixing of the chemical elements was modeled with the coherent potential approximation (CPA) [50,62,63], *i.e.*, the varying potentials in the random substitutional solid solution are replaced by an effective potential. Internal atomic positions were fixed to keep the rigid-sphere packing. For PAW-based calculations, supercells with random atomic occupations were considered and the atomic positions were allowed to relax. All calculations neglect short-range ordering effects. The equilibrium properties at 0 K were obtained by computing total energies with EMTO for 16 volumes in a range of 10 to 13 Å³/atom and by fitting the energy-volume functions to the Vinet equation of state [64,65].

3.1. Magnetic properties

Collinear spin polarization was considered to simulate different magnetic states for the alloys. We assumed that the magnetic

states are perfectly ordered or random, which represent the extreme limits. In the EMTO approach for Cantor-based HEAs, a ferrimagnetic (FiM) state, in which the magnetic moments of Cr and Mn are ordered parallel to each other and antiparallel to those of Fe, Co, and Ni ordered ferromagnetically (*cf*. Fig. S1a, hereafter referred to as FiM-I), has been previously adopted [66].

Recent studies [67,68], however, have revealed that some elements in Cantor-based HEAs energetically prefer an antiferromagnetic ordering with magnetic moments oriented alternately up and down along the <100> direction in the FCC crystal. Therefore, we considered two such magnetic orderings based on 4-atom conventional unit cells for the FCC phase. For the low-Cr alloys (x = 0, 5, 10, and 14 at.% in $Cr_xMn_{20}Fe_{20}Co_{20}Ni_{40-x}$), it is found that a magnetic state where the magnetic moments of Cr and Mn are ordered antiferromagnetically and the magnetic moments of Fe, Co, and Ni are ordered ferromagnetically (Fig. S1b, hereafter referred to as FiM-II) is lower in energy than the FiM-I state. In contrast, for the high-Cr alloys ($16 \leq x \leq 26$ at.%), the antiferromagnetic (AFM) state, *i.e.*, a state in which all magnetic moments are ordered antiferromagnetically (Fig. S1c) is found to be energetically more stable than FiM-I and FiM-II states. We considered in addition a paramagnetic (PM) state, where the magnetic moments are oriented randomly, as the ideal magnetic high-temperature limit by utilizing the disordered local moment (DLM) method [69,70] within the CPA formalism. Finally, a nonmagnetic state, *i.e.*, a state where even local magnetic moments are not present, was also considered as a reference energy to assess magnetic phase stability.

3.2. (Generalized) stacking fault energies

The intrinsic SFE (γ_{isf}) was calculated with EMTO for $Cr_xMn_{20}Fe_{20}Co_{20}Ni_{40-x}$ with x = 14, 16, 18, 20, 22, 24, 26 at.% at 0 K and 300 K in the DLM state. At 0 K, we employed FCC and faulted 1×1×6 supercells with the z-direction parallel to [111]. At 300 K, to consistently model finite temperature effects, we used the second-order axial Ising model [71]. We considered the theoretical equilibrium lattice parameter of the FCC phase for the given temperature and composition and included vibrational, magnetic, and electronic contributions in the Gibbs energies. The vibrational contribution was computed based on the Debye-Grüneisen model following Moruzzi *et al*. [72] (*cf*. Refs. [66] and [73]); the electronic excitations were calculated by applying the Fermi smearing; the magnetic state was modeled with the DLM method; the magnetic entropy was treated with the mean-field approximation for itinerant systems [74]

$$S_{magn} \approx 3k_B \sum_i \ln |m_i| \quad (2)$$

This approximation may be more appropriate than the standard Heisenberg model for Cr and Ni, therefore we chose this expression because we are varying the ratio of these elements in the Cantor alloy. Further details and a comparison with the approximation $S_{magn} = k_B \sum_i \ln(|m_i| + 1)$ for the present alloys are provided in the supplementary materials.

As the EMTO method strongly overestimates the unstable stacking fault energies because of the imperfect overlapping of the potential spheres due to open packing [75], the unstable SFEs were determined with the PAW method using 4×4×6 supercells with a random occupation of the atoms for the compositions $Cr_{12.9}Mn_{20.4}Fe_{20.4}Co_{20.4}Ni_{25.9}$ and $Cr_{25.9}Mn_{20.4}Fe_{20.4}Co_{20.4}Ni_{12.9}$. To obtain converged mean values and standard deviations for the stable and unstable SFEs, we utilized 40 and 20 different chemical arrangements for the two compositions, respectively. We employed a cutoff energy of 400 eV and a Methfessel-Paxton smearing [76] with a width of 0.1 eV. For each supercell, we fully relaxed the atomic positions of the FCC cells, then tilted the unit cell to create the stacking faults, and finally allowed for further relaxation only in the direction perpendicular to the fault. We sampled the GSFE-surface at six points and parametrized it using Eq. S14 [77] (further details are given in supplementary materials). For clarity, we summarize the advantages and disadvantages of the EMTO and PAW methods for HEAs in Table 1.

Table 1
Advantages and disadvantages of the two DFT approaches employed in this work. NM, FiM, and PM stand for non-magnetic, ferrimagnetic, and paramagnetic, respectively.

	EMTO	PAW
Chemical complexity	Approximated (CPA)	Explicit (supercells)
Atomic relaxations	No	Yes
Magnetic states	NM, FiM, PM	NM, FiM
Finite temperature effects	Yes	Yes, but expensive*
Short-range ordering	No	Yes, but expensive*
Computational effort	Low	High

* not considered here

We estimated the separation distance d between two Shockley partials with the generalized Peierls-Nabarro model [78–80]. Full details are provided in the supplementary materials.

4. Results

4.1. Composition and microstructure of as-cast and homogenized ingots

The chemical compositions of the ten cylindrical ingots were analyzed by EDX. Two metallographic cross-sections were taken from the top and the bottom of the cast ingots and chemical compositions were measured over areas of 0.25 mm^2 at different radial positions spaced 4 mm apart, see Figs. S3-S5 in supplementary materials. This procedure is similar to that in [35]. The analysis revealed that the ingots have homogeneous chemical compositions at the millimeter scale that are very close to the alloy compositions aimed for, see Table 2 (deviations were all below the accuracy of EDX: ± 0.5 at.%). Therefore, from here on, each alloy is denoted by its nominal (aimed for) composition in at.%.

EDX elemental maps were recorded after casting (left column in Fig. 1) and homogenization (right column). A representative example is given in Fig. 1 for the $Cr_5Mn_{20}Fe_{20}Co_{20}Ni_{35}$ alloy where the mean grain size exceeds 1 mm. After casting, the EDX elemental maps in the left column of Fig. 1 reveal clear evidence of chemical segregation with dendrites enriched in Cr, Fe, and Co and interdendritic regions enriched in Ni and Mn. In contrast, no chemical segregation could be detected after homogenization at 1473 K for 48 h, see right column of Fig. 1. Therefore, while the chemical analysis at the millimeter scale indicated homogeneous composition in the cast condition, EDX elemental maps in Fig. 1 show chemical segregation at the microscale, which can be completely

Table 2
Chemical compositions (in at.%) of the ten HEAs determined by EDX. The accuracy is ±0.5 at.%.

Nominal Composition	Cr	Mn	Fe	Co	Ni
$Mn_{20}Fe_{20}Co_{20}Ni_{40}$	0.3	19.8	20.4	19.9	39.6
$Cr_5Mn_{20}Fe_{20}Co_{20}Ni_{35}$	5.3	20.0	20.3	19.7	34.7
$Cr_{10}Mn_{20}Fe_{20}Co_{20}Ni_{30}$	9.8	20.1	20.2	19.7	30.2
$Cr_{14}Mn_{20}Fe_{20}Co_{20}Ni_{26}$	14.3	20.0	20.2	19.7	25.9
$Cr_{16}Mn_{20}Fe_{20}Co_{20}Ni_{24}$	16.3	20.2	19.7	19.9	23.9
$Cr_{18}Mn_{20}Fe_{20}Co_{20}Ni_{22}$	18.0	20.0	20.0	19.9	22.1
$Cr_{20}Mn_{20}Fe_{20}Co_{20}Ni_{20}$	19.9	20.1	20.3	19.8	19.9
$Cr_{22}Mn_{20}Fe_{20}Co_{20}Ni_{18}$	22.1	20.3	19.6	19.9	18.0
$Cr_{24}Mn_{20}Fe_{20}Co_{20}Ni_{16}$	24.0	20.1	19.7	20.0	16.2
$Cr_{26}Mn_{20}Fe_{20}Co_{20}Ni_{14}$	25.7	20.7	19.4	19.8	14.4

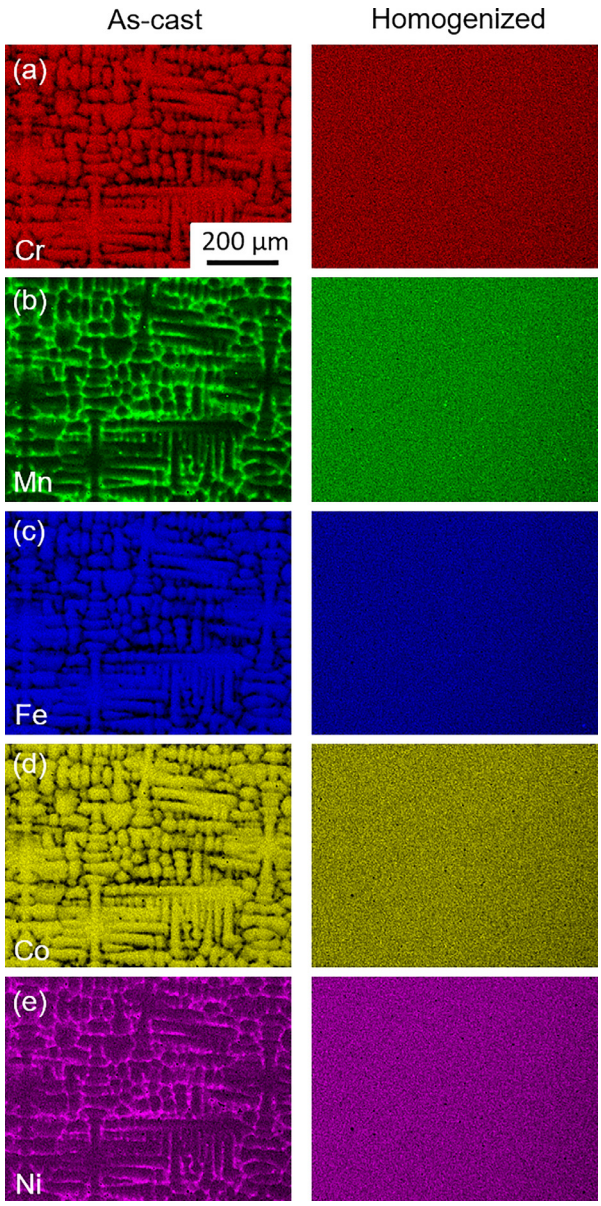

Fig. 1. Elemental EDX maps of the $Cr_5Mn_{20}Fe_{20}Co_{20}Ni_{35}$ alloy: (a) Cr, (b) Mn, (c) Fe, (d) Co, and (f) Ni in the as-cast condition (left column) and the homogenized state (right column). Similar elemental partitioning was observed in all the alloys investigated, as shown in supplementary materials.

homogenized after annealing at 1473 K for 48 h. Similar analyses were performed on all ten alloys and representative EDX elemental maps for Mn are provided in Figs. S6 and S7. In all cases, uniform elemental distributions were obtained after homogenization.

4.2. Lattice parameter, texture and mean grain size after recrystallization

After recrystallization at 1173 K for 1 h, only the two alloys with the highest Cr contents were two-phase with Cr-rich σ precipitates in an FCC matrix; the other HEAs were single-phase FCC. To dissolve σ precipitates in the 24 and 26 at.% Cr alloys, the pseudo-binary phase diagram reported by Laplanche *et al.* [31] was used to select a recrystallization temperature that was above the σ-phase solvus. The full list of annealing temperatures and durations is provided in Table 3.

For phase analyses, XRD and EBSD were performed. Two representative XRD patterns are shown in the left column of Fig. 2 for the alloys with (a) lowest and (b) highest Cr concentrations. Diffraction patterns for the other alloys can be found in supplementary materials, Fig. S8. All XRD patterns showed the typical peaks of a disordered FCC solid solution; no additional peaks of secondary phases were detected. From the XRD patterns, the FCC lattice parameters of the ten alloys were determined by Rietveld analysis using the MAUD program [81] and are listed in Table 3. The lattice parameter $a_{exp} \approx 0.3599$ nm is found to be roughly independent of composition in the investigated concentration range. This trend is found also in the theoretical lattice parameters at 0 K and 300 K computed with the EMTO method with the exception of the $Mn_{20}Fe_{20}Co_{20}Ni_{40}$ and $Cr_5Mn_{20}Fe_{20}Co_{20}Ni_{35}$ alloys, which have a slightly larger lattice constant, see a_{th} values in Table 3. The theoretical lattice parameters at 300 K are underestimated by roughly 0.8% with respect to the experimental ones; we attribute this discrepancy to the neglection of anharmonic vibrations and to the approximations of the EMTO method.

Representative grain orientation maps with an overlaid image quality map (bright/dark contrast) for the $Mn_{20}Fe_{20}Co_{20}Ni_{40}$ and $Cr_{26}Mn_{20}Fe_{20}Co_{20}Ni_{14}$ alloys are shown in the middle column of Fig. 2. In these EBSD images, the color of each crystallite indicates the crystallographic direction parallel to the rod axis (see white arrows). The stereographic triangle in the middle column of Fig. 2a can be used to translate the colors into crystallographic orientations parallel to the rod axis. The stereographic triangles in the right column of Fig. 2 are IPFs showing the texture along the rod axis, expressed in multiple times random. The corresponding greyscale can be found at the top right of Fig. 2. The IPFs reveal that there is only a weak texture after swaging and recrystallization.

Table 3
Recrystallization heat treatments, resulting grain sizes (D), FCC lattice parameters from experiments (a_{exp}) and theory (a_{th}), mass density (ρ), and coefficient of true thermal expansion (α) at RT of the single-phase FCC HEAs investigated in this study. In the case of α, the standard deviations obtained from fitting 4th-order polynomials to the observed thermal strain curves are given as the experimental scatter. The reproducibility in successive runs is usually of order $0.05 \cdot 10^{-6} K^{-1}$.

nominal compositions/at.%	annealing temperature/K	annealing duration/min	D/µm	a_{exp}/nm (300 K)	a_{th}/nm(0 K)	a_{th}/nm(300 K)	ρ/g cm^{-3}	$\alpha \times 10^6/K^{-1}$
exp. scatter			± 6%	± 0.2%			± 0.1%	± 0.1%
$Mn_{20}Fe_{20}Co_{20}Ni_{40}$	1173	60	27	0.36007	0.3549	-	8.16	13.28
$Cr_5Mn_{20}Fe_{20}Co_{20}Ni_{35}$	1173	60	25	0.35985	0.3541	-	8.12	14.79
$Cr_{10}Mn_{20}Fe_{20}Co_{20}Ni_{30}$	1173	60	22	0.35983	0.3534	-	8.11	15.44
$Cr_{14}Mn_{20}Fe_{20}Co_{20}Ni_{26}$	1173	60	18	0.35969	0.3530	0.3572	7.98	16.01
$Cr_{16}Mn_{20}Fe_{20}Co_{20}Ni_{24}$	1173	60	18	0.35976	0.3529	0.3572	7.95	15.96
$Cr_{18}Mn_{20}Fe_{20}Co_{20}Ni_{22}$	1173	60	19	0.35981	0.3529	0.3572	7.94	15.99
$Cr_{20}Mn_{20}Fe_{20}Co_{20}Ni_{20}$	1173	60	18	0.36000	0.3528	0.3571	7.92	15.70
$Cr_{22}Mn_{20}Fe_{20}Co_{20}Ni_{18}$	1173	60	19	0.36004	0.3528	0.3572	7.89	15.84
$Cr_{24}Mn_{20}Fe_{20}Co_{20}Ni_{16}$	1273	5	22	0.36005	0.3529	0.3572	7.90	15.79
$Cr_{26}Mn_{20}Fe_{20}Co_{20}Ni_{14}$	1373	15	61	0.36015	0.3529	0.3572	7.87	15.77

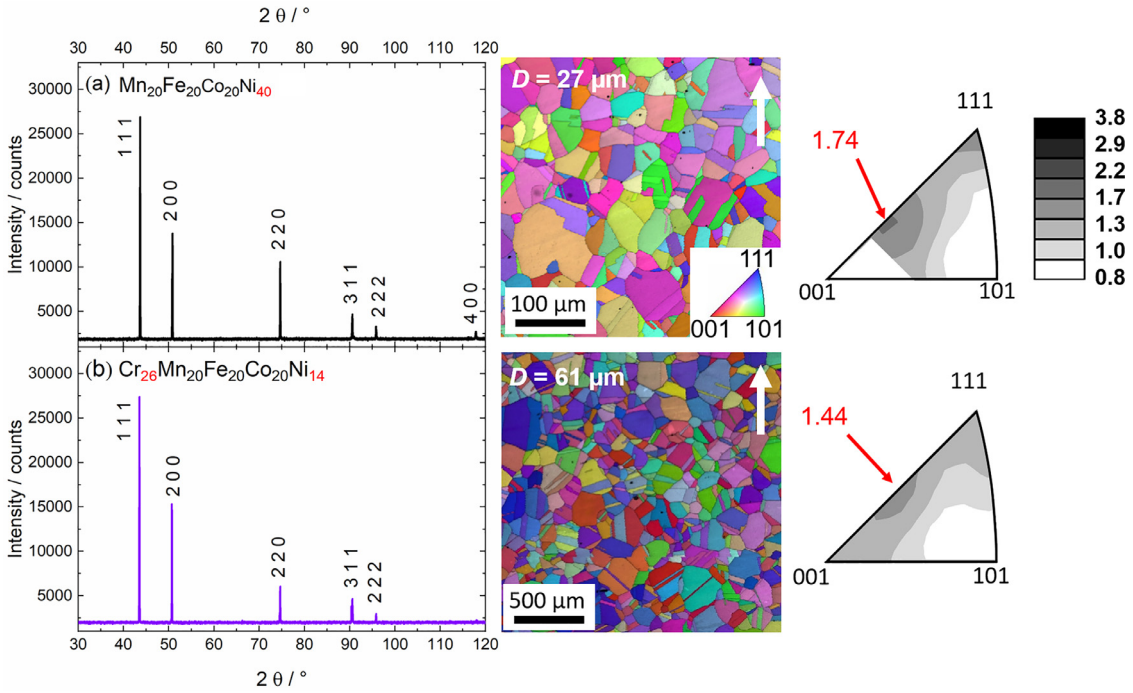

Fig. 2. Phase and microstructural analyses of the cold-worked and recrystallized HEAs (a) $Mn_{20}Fe_{20}Co_{20}Ni_{40}$, lowest Cr concentration, and (b) $Cr_{26}Mn_{20}Fe_{20}Co_{20}Ni_{14}$, highest Cr concentration. Figures in the left column are XRD patterns, those in the middle are color-coded grain orientation maps, and those in the right column are inverse pole figures showing weak texture parallel to the rod axis (indicated by the white arrow in the upper right corner of the EBSD images). The scale of the IPFs is shown at the top right and the maximum pole density of each IPF is indicated with a red arrow.

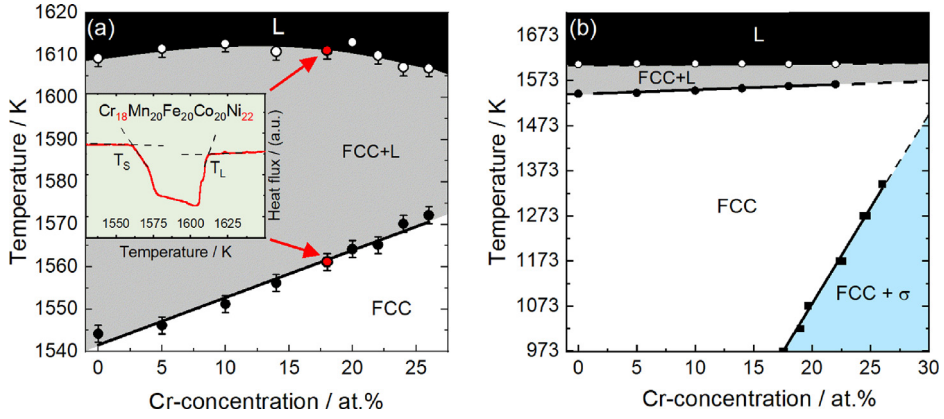

Fig. 3. Melting range as a function of composition in $Cr_xMn_{20}Fe_{20}Co_{20}Ni_{40-x}$ alloys ($0 \leq x \leq 26$ at.%). (a) Solidus and liquidus temperatures determined by DSC as a function of Cr concentration. The inset is a representative DSC heating curve in which the endothermic event represents the melting range of the $Cr_{18}Mn_{20}Fe_{20}Co_{20}Ni_{22}$ HEA. Using a tangent method, the solidus (T_S) and liquidus (T_L) temperatures were determined at the onset and end of the endothermic peak. (b) Pseudo-binary phase diagram summarizing the melting range of CrMnFeCoNi HEAs as a function of temperature from the present work as well as the phase-stability data down to 973 K reported by Laplanche et al. [31].

As shown in the middle column of Fig. 2, the grains are equiaxed and contain several annealing twins. Their sizes were found to be relatively homogeneous throughout the recrystallized rods and the average grain size of each alloy is listed in Table 3. The mean grain sizes of the eight alloys with the lowest Cr contents, which were recrystallized at 1173 K for 1 h, lie in the range 18 to 27 µm. The two alloys with higher Cr concentrations were annealed at higher temperatures to obtain a single-phase FCC microstructure. In an effort to keep their grain size roughly the same as that of the others, the duration of the anneals was reduced. This resulted in a grain size of 22 µm for $Cr_{24}Mn_{20}Fe_{20}Co_{20}Ni_{16}$; however, the minimum grain size achievable in $Cr_{26}Mn_{20}Fe_{20}Co_{20}Ni_{14}$ was 61 µm, see Table 3. Nevertheless, the physical properties reported in the present study should not be affected by variations of grain size in the range 18 to 61 µm.

4.3. Thermal analysis

A representative DSC heating curve for $Cr_{18}Mn_{20}Fe_{20}Co_{20}Ni_{22}$ is shown as an inset in Fig. 3a. The solidus (T_S) and liquidus (T_L) temperatures were determined by the intersection of fitted tangents (dashed lines) at the onset and end of the endothermic event. For the equiatomic $Cr_{20}Mn_{20}Fe_{20}Co_{20}Ni_{20}$ HEA, our melting range (1564–1613 K) is consistent with those reported in the literature, *e.g.*, (1553–1622 K) [13], (1562–1612 K) [82], (1563–1613 K) [83]. With increasing Cr content from 0 to 26 at.%, T_S increases by ~30 K while the T_L remains roughly constant. Correspondingly, the width

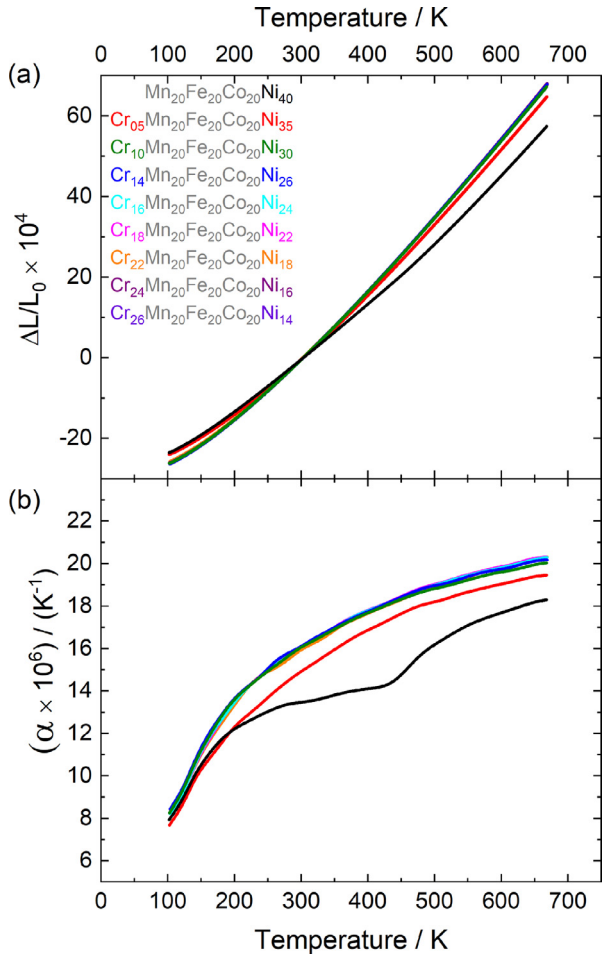

Fig. 4. Thermal expansion behavior of the investigated alloys. (a) Experimentally observed strains $\varepsilon(T) = \Delta L/L_0$ and (b) thermal expansion coefficient $\alpha(T) = \partial\varepsilon/\partial T$.

of the solidification range (and thus the susceptibility to dendritic solidification) decreases with increasing Cr/Ni ratio.

4.4. Thermal expansion

The temperature-induced strains $\varepsilon(T) = (L(T) - L_0)/L_0$ of the recrystallized alloys, where L_0 is the sample length at 295 K, are shown in Fig. 4a. Except for the two alloys with the highest Ni contents, which expand less in the investigated temperature range, all the other alloys exhibit nearly the same thermal expansion behavior. This becomes even more evident in the plot of the temperature dependence of the thermal expansion coefficients $\alpha = \partial\varepsilon/\partial T$ (Fig. 4b) and the RT coefficients listed in Table 3. The $\alpha(T)$ curves are identical within experimental error for the HEAs with $x \geq 10$ at.%; however, those of $Mn_{20}Fe_{20}Co_{20}Ni_{40}$ and $Cr_5Mn_{20}Fe_{20}Co_{20}Ni_{35}$ are systematically lower in the whole temperature range. Below 200 K, $Mn_{20}Fe_{20}Co_{20}Ni_{40}$ and $Cr_5Mn_{20}Fe_{20}Co_{20}Ni_{35}$ exhibit roughly the same coefficient of thermal expansion but between 200 and 440 K the curve of the Cr-free alloy flattens before an abrupt steep increase at about 440 K.

4.5. Elastic properties

The experimental elastic stiffness coefficients and moduli at RT are given in Table 4. Figs. 5a and 5b depict the temperature dependencies of the shear and Young's moduli, respectively. The experimental data points of G and E were fitted using Varshni's equation

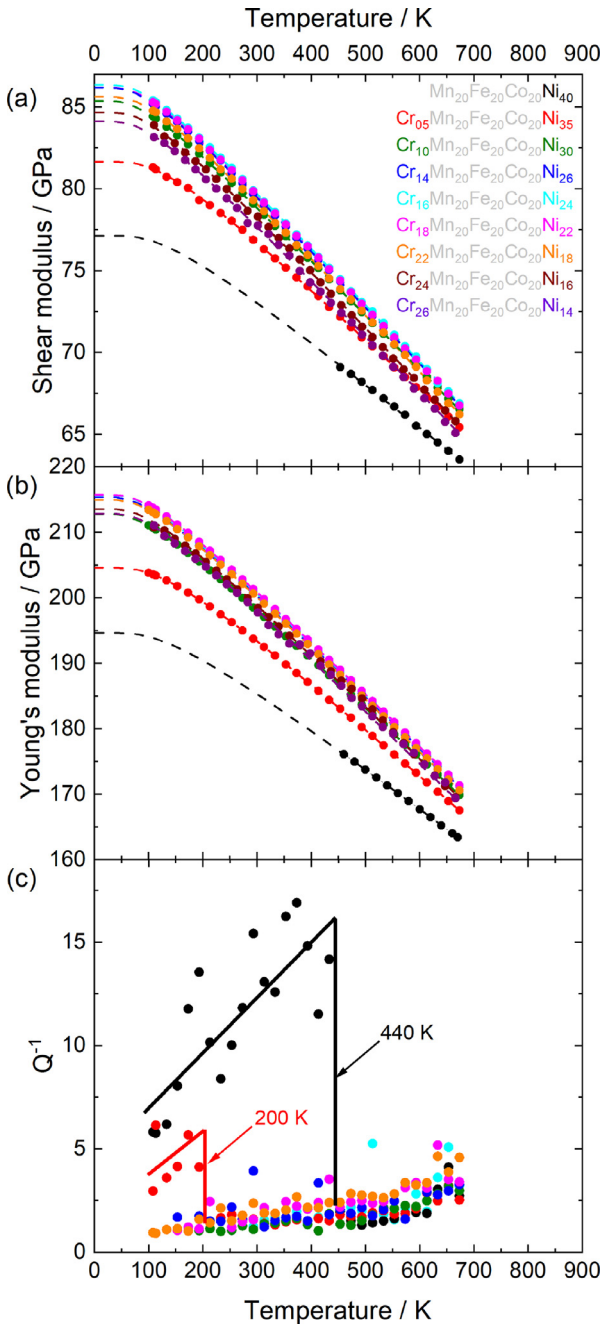

Fig. 5. Temperature dependence of elastic properties. (a) Shear modulus, (b) Young's modulus, and (c) inverse quality factor Q^{-1} of selected eigen modes. In (a) and (b), dots represent measured points, dashed lines are fits using Varshni's equation [39], see Eqs. S3, S4 and fitting parameters in Table 4.

[39] (see Eqs. S3, S4) and the best fits are represented by dashed lines in Fig. 5, while the fit parameters are listed in Table 4. Also shown in Table 4 are the data reported for the equiatomic alloy in Ref. [84]. The ultrasound attenuation (Q^{-1}) with temperature is presented in Fig. 5c. Except for the two alloys with the highest Ni content, the anelastic losses are relatively low in the investigated frequency range. Only in the case of $Mn_{20}Fe_{20}Co_{20}Ni_{40}$ was the damping so strong that, below about 440 K, no reliable elastic stiffnesses could be obtained. The relatively large grain size of the $Cr_{26}Mn_{20}Fe_{20}Co_{20}Ni_{14}$ HEA (see Table 3) may have had some influence on its resonance spectrum. Therefore, the uncertainties in E and G of this alloy were estimated to be twice those of the other alloys.

Table 4
Elastic stiffness coefficients c_{11}, c_{12}, and $c_{44} = (c_{11} - c_{12})/2$, shear modulus ($G$), Young's modulus ($E$), and Poisson's ratio ($\nu$) determined at RT. Additionally, the parameters E^0, s_E, T_E and G^0, s_G, T_G obtained by fitting Varshni's equation [39] to the experimental Young's and shear moduli are given (*cf.* Figs. 5a,b).

Alloy	c_{11}/GPa	c_{12}/GPa	$c_{44} = G$/GPa	$E = s_{11}^{-1}$/GPa	ν/-	E^0/GPa	s_E/GPa	T_E/K	G^0/GPa	s_G/GPa	T_G/K
	Experimental data at room temperature					Varshni's parameters [39] for $E(T)$ and $G(T)$					
Uncertainty	±3%	±3%	±3%	±3%	±20%	±4%	±2%	±2%	±1.25%	±1%	±1%
$Mn_{20}Fe_{20}Co_{20}Ni_{40}$	210.9	65.7	72.6	185.5	0.265	194	27.6	433	77.1	12.0	436
$Cr_5Mn_{20}Fe_{20}Co_{20}Ni_{35}$	236.6	82.9	76.9	193.8	0.260	205	26.7	366	81.7	11.3	355
$Cr_{10}Mn_{20}Fe_{20}Co_{20}Ni_{30}$	241.5	83.3	79.1	198.5	0.256	213	20.2	261	85.1	9.4	274
$Cr_{14}Mn_{20}Fe_{20}Co_{20}Ni_{26}$	243.3	85.2	79.1	200.8	0.260	215	21.2	265	86.0	9.5	270
$Cr_{16}Mn_{20}Fe_{20}Co_{20}Ni_{24}$	243.5	85.0	79.3	201.2	0.259	216	22.1	274	86.3	9.5	268
$Cr_{18}Mn_{20}Fe_{20}Co_{20}Ni_{22}$	244.8	86.0	79.4	201.3	0.261	215	22.9	281	86.2	9.5	268
$Cr_{20}Mn_{20}Fe_{20}Co_{20}Ni_{20}$	-	-	81*	203*	0.25*	214*	35*	416*	85*	16*	448*
$Cr_{22}Mn_{20}Fe_{20}Co_{20}Ni_{18}$	246.5	89.3	78.6	200.6	0.265	215	23.1	283	85.6	9.5	268
$Cr_{24}Mn_{20}Fe_{20}Co_{20}Ni_{16}$	248.6	91.7	78.4	198.4	0.267	213	21.5	270	84.6	10.0	283
$Cr_{26}Mn_{20}Fe_{20}Co_{20}Ni_{14}$	250.5	94.6	78.0	197.8	0.273	213	20.7	265	83.9	10.5	296

* value reported in Ref. [84] using a different resonance-based method.

For $Cr_xMn_{20}Fe_{20}Co_{20}Ni_{40-x}$ alloys with $x \geq 10$ at.%, the magnitude and temperature dependence of the elastic moduli vary only slightly (Figs. 5a and 5b). The observed softening of the elastic moduli with increasing temperature can be well described by Varshni's equation [39], which is based on an Einstein model for the vibrational behavior of the alloy. Such a temperature dependence is common in HEAs [84–87] and MEAs [38,40,88]. However, alloys with Cr contents $\leq$ 10 at.% are significantly softer. For example, the shear moduli of $Cr_5Mn_{20}Fe_{20}Co_{20}Ni_{35}$ and $Mn_{20}Fe_{20}Co_{20}Ni_{40}$ are ~4% and ~10% lower at RT compared to the other alloys, see Fig. 5b. The Cr concentration also affects the internal friction of the alloys (Fig. 5c). For $x \geq 10$ at.%, the inverse quality factor of resonances in the frequency regime 100 – 800 kHz is relatively low and decreases almost linearly with decreasing temperature. In contrast, for $Cr_5Mn_{20}Fe_{20}Co_{20}Ni_{35}$ and $Mn_{20}Fe_{20}Co_{20}Ni_{40}$, the ultrasound attenuation suddenly increases at ~200 K and 440 K, respectively, followed by a linear decrease with decreasing temperature. Such abrupt changes of Q^{-1} are likely induced by phase transitions as discussed in the next section.

4.6. Magnetic properties

To identify the processes responsible for the discontinuities observed on the $\alpha(T)$ and $Q^{-1}(T)$ curves (Figs. 4b and 5c), we studied the magnetic behavior of all alloys at 293 K and as a function of temperature in the case of the $Mn_{20}Fe_{20}Co_{20}Ni_{40}$ alloy using a thermobalance as described in Section 2.4. At 293 K, most of the alloys were nonmagnetic but $Cr_5Mn_{20}Fe_{20}Co_{20}Ni_{35}$ and $Mn_{20}Fe_{20}Co_{20}Ni_{40}$ were slightly and strongly magnetic, respectively. The apparent weight of the latter alloy decreased sharply at ~450 K (Fig. 6), *i.e.*, at this (Curie) temperature, the attraction to the magnet of the thermobalance disappeared corresponding to a loss of the alloy's permanent magnetism. The Curie temperature is consistent with the discontinuities observed at ~440 K on the $\alpha(T)$ and $Q^{-1}(T)$ curves of $Mn_{20}Fe_{20}Co_{20}Ni_{40}$ (Figs. 4b and 5c). The difference of about 10 K may be related to the fact that different heating rates were used for thermogravimetric analysis (5 K/min), dilatation experiments (2 K/min), and elastic moduli measurements (data collection at discrete isothermal steps). Therefore, it can be concluded that the Curie temperature of the $Mn_{20}Fe_{20}Co_{20}Ni_{40}$ alloy is ~440 K. When Cr is added at the expense of Ni to produce the $Cr_5Mn_{20}Fe_{20}Co_{20}Ni_{35}$ HEA, the overall magnetism of the alloy as well as the magnitude of the magnetic to nonmagnetic transition is decreased as Cr is antiferromagnetic. Consistent with this view, the increase in inverse quality factor in Fig. 5c is much stronger for the Cr-free alloy than for the $Cr_5Mn_{20}Fe_{20}Co_{20}Ni_{35}$ HEA. However, in the case of the dilatation measurements, while a clear discontinuity was observed in Fig. 4b for the Cr-free alloy at the Curie temperature, the magnetic transition in the $Cr_5Mn_{20}Fe_{20}Co_{20}Ni_{35}$ alloy is probably too weak to yield a measurable signal in Fig. 4b. Based on these observations, we suggest that the Curie temperature of the $Cr_5Mn_{20}Fe_{20}Co_{20}Ni_{35}$ HEA is ~200 K, while those of the other alloys, if they have one, are lower than 100 K (the lowest temperature investigated here). Schneeweiss *et al.* [67] observed a ferromagnetic transition at 38 K in the equiatomic $Cr_{20}Mn_{20}Fe_{20}Co_{20}Ni_{20}$ HEA; similar low-temperature data do not exist for the other alloys.

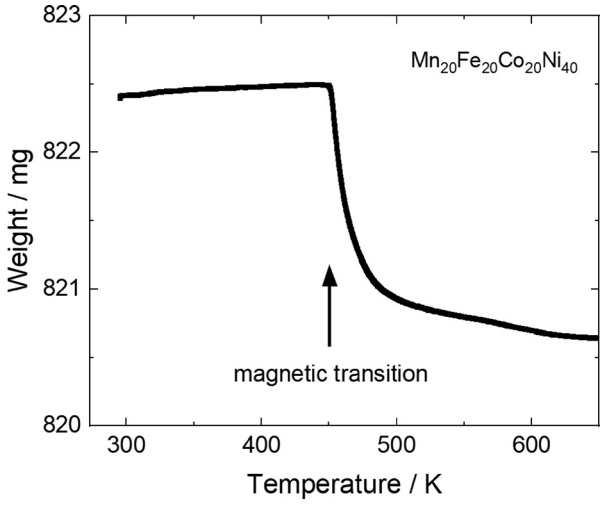

Fig. 6. Apparent weight of the $Mn_{20}Fe_{20}Co_{20}Ni_{40}$ alloy, resulting from the sum of gravitational and magnetic forces, as a function of temperature. The weight reduction at 450 K marks the loss of magnetic interactions.

4.7. Magnetic state simulation and expansion anomaly

The *ab initio* computed enthalpy differences relative to the nonmagnetic phase at 0 K are shown in Fig. 7a. For the alloys with low Cr concentrations, $0 \leq x \leq 14$ at.%, the FiM-II state (*cf.* Fig. S1) is found to be lower in energy than the FiM-I and AFM states, see orange full line in Fig. 7a. This suggests that the magnetic transition observed in Fig. 6 is ferrimagnetic ↔ paramagnetic but it must be emphasized that this is a simplified view and the real nature of magnetic transitions in HEAs is probably more complex. For higher Cr concentrations, $16 \leq x \leq 26$ at.%, the AFM state (green full line) is found to be energetically more favorable, Fig. 7a. In the following, we therefore consider the FiM-II and the AFM states for $x < 15$ and $x > 15$ at.%, respectively, as magnetic ground states. The energetically favorable magnetic state at low temperatures is needed to estimate the magnetic critical temperature, T_c, of the considered alloys. We compute T_c based on a mean-field approximation (MFA)

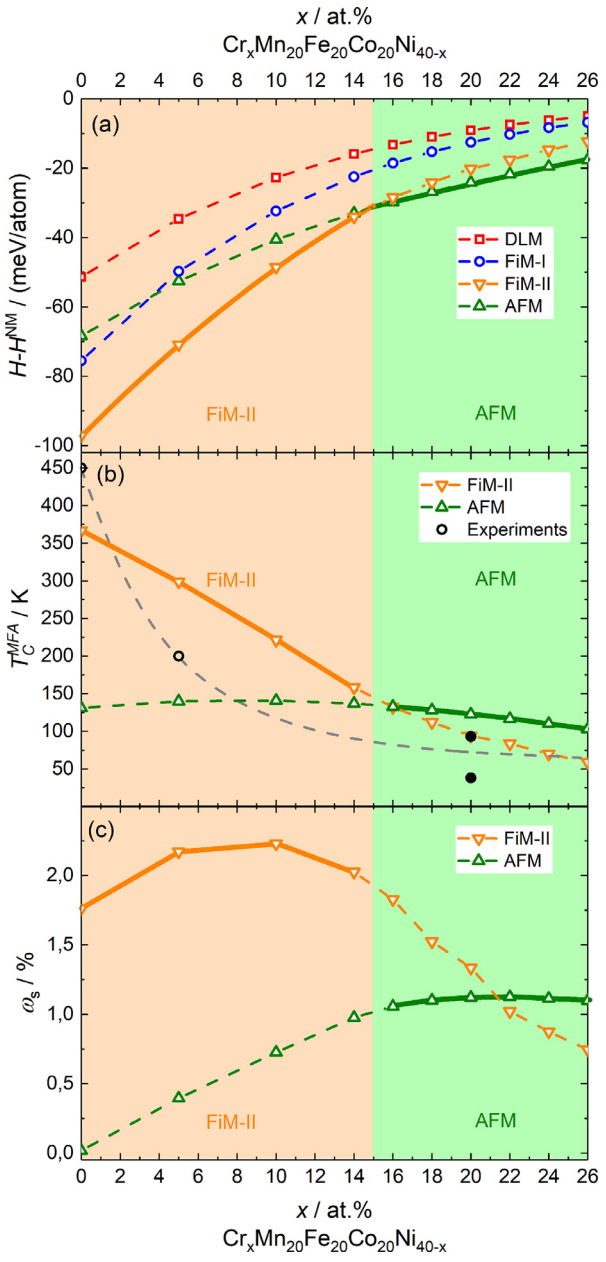

Fig. 7. (a) *Ab initio* computed enthalpy differences from the nonmagnetic phase at 0 K including a paramagnetic state (DLM, red), the FiM-I (blue), FiM-II (orange), and AFM (green) states shown in Fig. S1. Background colors distinguish the magnetically more favorable state at a given composition. (b) *Ab initio* computed magnetic critical temperature in the mean-field approximation. The experimental Curie temperatures (black circles in (b)) were obtained in the present study for the $Cr_5Mn_{20}Fe_{20}Co_{20}Ni_{35}$ and $Mn_{20}Fe_{20}Co_{20}Ni_{40}$ and the filled black data points for the Cantor alloy were taken from Ref. [67]. (c) *Ab initio* computed spontaneous volume magnetostriction ω_s. Dashed curves indicate that other magnetic states are found higher in energy at the composition while the full lines highlight the most energetically favorable magnetic states.

[89] as

$$T_c^{MFA} = \frac{2}{3\ k_B}\left(E^{DLM} - E^{MGS}\right), \tag{3}$$

where E^{DLM} and E^{MGS} denote the energies of the paramagnetic (DLM) and magnetic ground states, respectively. Mean-field approaches, which are based on a theory of idealized localized spins (local moments), usually tend to overestimate magnetic critical temperatures. The *ab initio* computed T_c^{MFA} is shown in Fig. 7b. The obtained values are 367 K, 299 K, and 123 K for $x = 0$, 5, and 20 at.%, respectively, see Fig. 7b. For the present alloys, the trend of the computed T_c is consistent with the experimental observations (450 K, 200 K, and 48 K for $x = 0$, 5, and 20 at.%, respectively) though the computed values overestimate the experimental values for $5 \leq x \leq 26$ at.% and underestimate the experimental T_c by about 80 K for the Cr-free alloy ($T_c^{exp} = 450$ K). We attribute this latter underestimation to the large amount of Ni (40 at.%), for which the idealized "local magnetic moment" picture may be limited due to strong longitudinal fluctuations [90]. For higher Cr concentrations, $x > 15$ at.%, the computed T_c^{MFA} values are found to be around 150 K, which indicates that at RT these alloys can be considered in the PM state, consistent with the present experimental data.

Our experimental data reveal a lower thermal expansion coefficient for the Cr-free alloy below T_c that suddenly increases above T_c (see black curve in Fig. 4b with steep increase at ~440 K), indicating a suppression of the expansion coefficient due to magnetism. Therefore, we investigated whether there are some indications of a potential magneto-volume effect, characteristic for Invar alloys [91] by examining the spontaneous volume magnetostriction ω_s given in a previous study [91] as

$$\omega_s = \frac{V^{MGS} - V^{DLM}}{V^{DLM}} \tag{4}$$

where V^{DLM} and V^{MGS} are the equilibrium volumes derived from the DFT calculations in the paramagnetic (DLM) and the magnetic ground state, respectively. The results are shown in Fig. 7c. Larger ω_s are found for alloys with low Cr concentrations ($x = 0$, 5, 10, 14 at.%), for which the FiM-II state is the magnetic ground state, compared with alloys containing more Cr, which have the AFM state as magnetic ground state. This implies that the alloys with low Cr concentrations may show a magneto-volume effect. For added perspective, the ω_s values of the investigated alloys (~1 - 2%) are smaller than those previously found in equiatomic FeCoNi and the super Invar $Fe_{63}Ni_{32}Co_5$ alloy (2.6 and 4.1%) [92], which is consistent with the much smaller impact on expansion found for the present alloy.

4.8. Burgers vector analysis

The diffraction pattern of a grain with the (111) plane parallel to the TEM foil is shown in Fig. 8a. Long dissociated dislocations can be observed in the corresponding bright-field scanning TEM (STEM) image obtained in multi-beam condition, Fig. 8b. The nature of these dissociated dislocations was determined using $\boldsymbol{g} \cdot \boldsymbol{b}$ analysis and the invisibility criterion $\boldsymbol{g} \cdot \boldsymbol{b} = 0$. The dissociated dislocation marked with a white dashed frame in Fig. 8b is magnified in Figs. 8c-e and imaged using the $\boldsymbol{g}(3\boldsymbol{g})$ WBDF technique with the three independent $\boldsymbol{g}$-vectors shown in Fig. 8a. Using the diffraction vector $\boldsymbol{g_1}$, which is parallel to $[02\bar{2}]$, only the upper partial dislocation is visible in Fig. 8c. With $\boldsymbol{g_2} = [20\bar{2}]$, the lower Shockley partial is visible in Fig. 8d. In contrast, both Shockley partials are visible with $\boldsymbol{g_3} = [2\bar{2}0]$ in Fig. 8e where the lower partial dislocation appears brighter because the strain field between the Shockley partials is different from that outside [44]. From this $\boldsymbol{g} \cdot \boldsymbol{b}$ analysis, the following conclusions can be drawn: (1) the Burgers vector of the perfect (undissociated) dislocation is parallel to $\boldsymbol{g_3}$ and thus equal to $a/2\ [1\bar{1}0]$, (2) the dislocation has a ~60° character and (3) it is dissociated into two Shockley partials according to the following reaction:

$$\frac{a}{2}[1\bar{1}0] = \frac{a}{6}[1\bar{2}1] + \frac{a}{6}[2\bar{1}\bar{1}]. \tag{5}$$

4.9. Stacking fault energies (SFEs) determined by TEM

The stacking fault energies (SFEs) of six of the investigated HEAs ($x = 14$, 18, 20, 22, 24, and 26 at.%) were obtained by

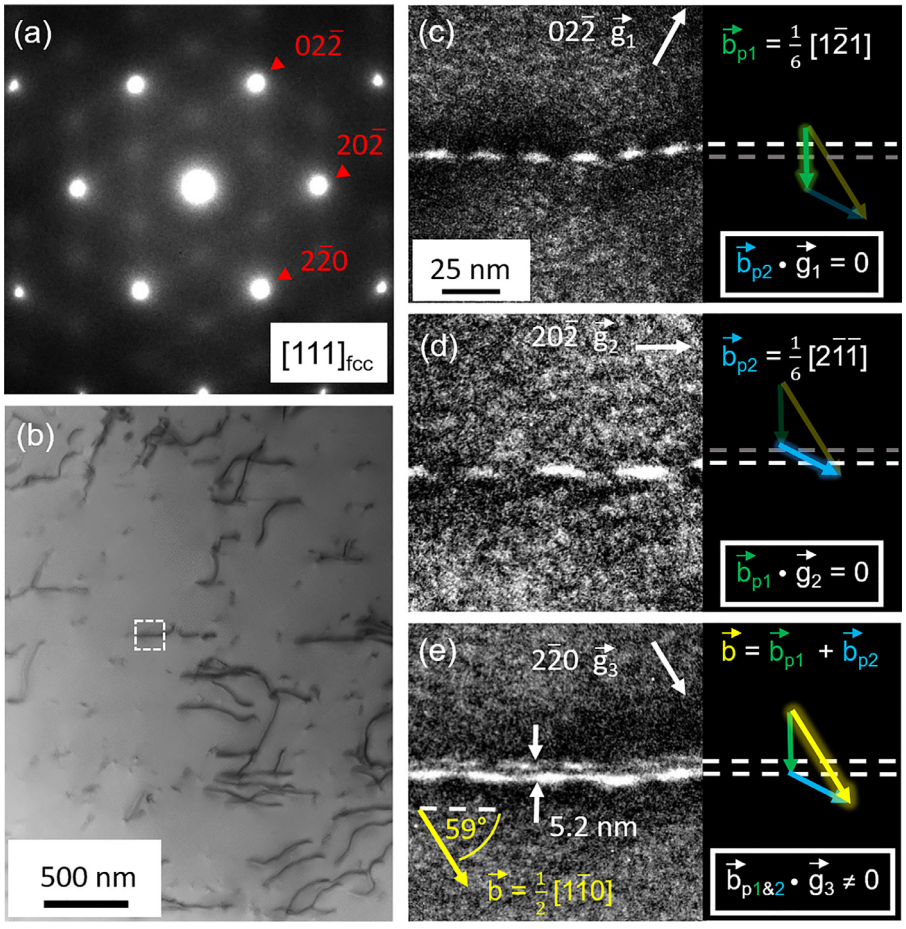

Fig. 8. Dislocation analysis after RT compression to 4% plastic strain. (a) Diffraction pattern showing that the (111) plane is almost parallel to the TEM foil. (b) STEM image showing an overview of the microstructure after deformation. (c-e) WBDF micrographs of a dissociated dislocation in three different $\boldsymbol{g}(3\boldsymbol{g})$-diffraction conditions. The schematics on the right side illustrate the (in)visibility of the partial dislocations and their Burgers vectors.

applying the TEM-based methodology developed by Cockayne *et al.* [43,44]. No dissociation could be detected for alloys with low Cr concentrations ($x \leq 10$ at.%) due to insufficient resolution of the WBDF technique when the TEM is operated at 200 kV. Representative actual partial separation distances (d) are shown in Fig. 9a for $Cr_{26}Mn_{20}Fe_{20}Co_{20}Ni_{14}$ (lowest SFE, black) and $Cr_{14}Mn_{20}Fe_{20}Co_{20}Ni_{26}$ (highest measurable SFE, red) as a function of the angle β between the dislocation line and the Burgers vector of the perfect dislocation. The rest of the experimental results are shown in Fig. S9 of the supplementary materials. Over the entire range of β, the Shockley partial separations for $Cr_{26}Mn_{20}Fe_{20}Co_{20}Ni_{14}$ (5–9 nm) are significantly higher than those for $Cr_{14}Mn_{20}Fe_{20}Co_{20}Ni_{26}$ (1.5 – 3 nm), indicating that the latter has a much higher SFE. From the measured separation distances at different angles, those for $\beta = 90°$ are plotted in Fig. 9b in black as a function of composition and will be compared to *ab initio* computations in Section 4.11.

Using the Burgers vector of the partials deduced from the measured lattice parameter, and the measured G and ν values, the $d(\beta)$-data points (Figs. 9a and S9) were fitted with the method of weighted least squares to the textbook equation (Eq. S10) for Volterra dislocations [42] by refining γ_{isf}. The best fits are represented by dashed lines in Fig. 9a. Upper and lower bounds encompassing all the data points were also computed using the same equation and the corresponding ranges are shown as shaded areas in Fig. 9a, which allows error bars of γ_{isf} to be estimated. The experimental SFEs thus obtained are displayed in Fig. 9c in black. They decrease linearly with increasing Cr/Ni ratio from about ~70 mJ/m² in $Cr_{14}Mn_{20}Fe_{20}Co_{20}Ni_{26}$ to ~20 mJ/m² in $Cr_{26}Mn_{20}Fe_{20}Co_{20}Ni_{14}$. Since the SFE is inversely proportional to the distance between partials, the error bars increase as the latter decreases, especially as the resolution limit of WBDF is approached. Our experimental data show a similar trend as those measured by Zaddach *et al.* [24] using XRD, *i.e.*, SFE decreases with increasing Cr/Ni ratio. However, our SFEs are generally higher. This difference may be due to several uncertainties in the SFE measurements of Zaddach *et al.* [24], which were mentioned in the introduction.

4.10. SFE simulation

The computed SFEs for $14 \leq x \leq 26$ at.% are displayed in Fig. 9c. In all cases, the SFE decreases with increasing Cr/Ni ratio, in agreement with the experiments. The relaxed PAW data (filled red squares in Fig. 9c) are within 1–1.5 standard deviations of the experimental data, even though a ferrimagnetic state at 0 K is modeled in these calculations. In contrast, the (unrelaxed) EMTO data at 0 K (empty blue squares in Fig. 9c) are much lower and the effect of Cr/Ni ratio on SFE is steeper than for the experimental curve, despite a more appropriate paramagnetic (DLM) state being considered. However, when finite temperature contributions at 300 K are included (vibrational and electronic free energies, thermal expansion, and magnetic entropy; filled blue squares in Fig. 9c) the computed SFEs move closer to the experimental ones. Nevertheless, the computed SFEs are still systematically lower by ~45 mJ/m².

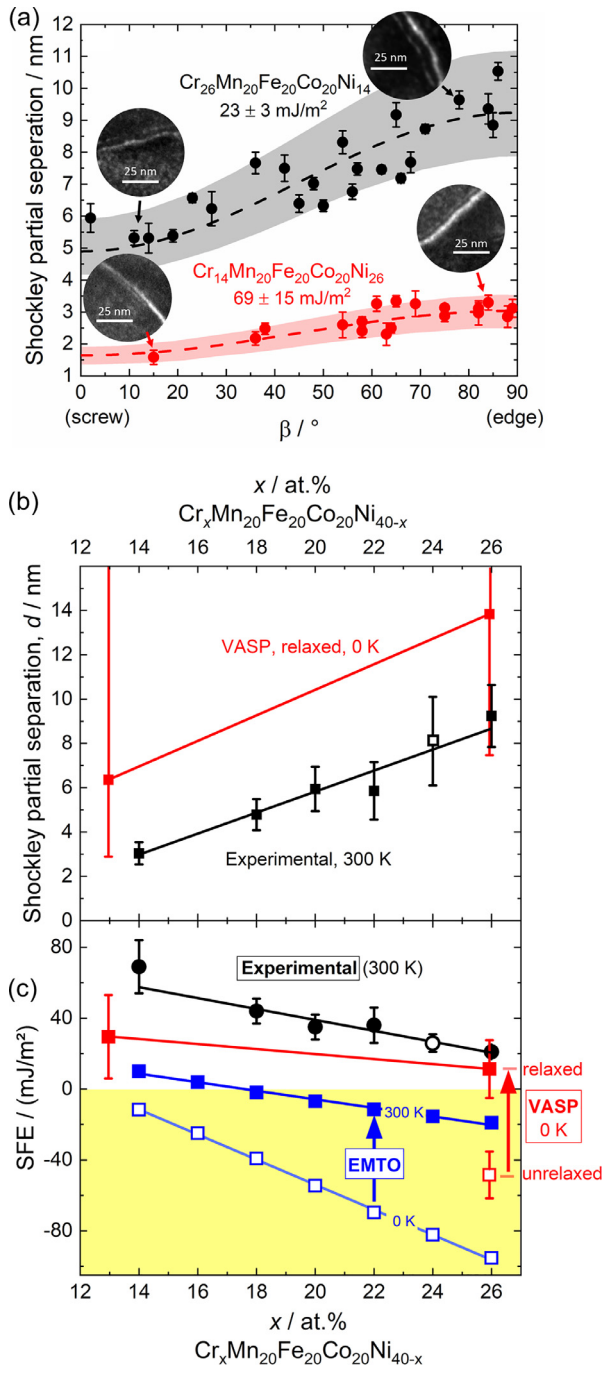

Fig. 9. (a) Shockley partial separation distances measured using the WBDF technique as a function of the angle β (dislocation character) for two HEAs. The insets show selected Shockley partial pairs. (b) Shockley partial separation distances as a function of composition for $\beta = 90°$ Black: measured using the WBDF technique at RT. Red: Calculated using the Peierls-Nabarro model in combination with the PAW method ("VASP") at 0 K. (c) Stacking fault energy of the HEAs *versus* Cr content. Black: experimental (all data for single-phase FCC alloys, except the empty circle that is for a two-phase σ + FCC $Cr_{26}Mn_{20}Fe_{20}Co_{20}Ni_{14}$ HEA, whose FCC matrix contains ~24 at.% Cr). Red: computed at 0 K with the PAW method ("VASP") in the ferrimagnetic state (relaxed and unrelaxed data are reported). Blue: computed at 0 K and 300 K with the EMTO method in the paramagnetic (DLM) state.

Additional EMTO calculations of the SFEs in the FiM-II magnetic state (not shown here) reveal a similar compositional trend as the EMTO data at 300 K for the DLM state but the overall SFEs are shifted higher by about 50 to 60 mJ/m^2. Magnetic and chemical SRO, if present, may further increase the derived SFEs. There are various possible reasons for the difference in SFEs derived from theory and experiments, which we will discuss in Section 5.3. Meanwhile, an important outcome of the present study is the demonstration of the shortcomings of EMTO in which atomic relaxations are not taken into account. In this regard, at least for the PAW data, this neglect causes a downward shift by as much as ~60 mJ/m^2 (compare filled and empty red squares in Fig. 9c) and we therefore speculate that an inclusion of relaxation energies would lead to a much better agreement of the EMTO and experimental data.

4.11. Comparison of experimental and ab initio computed Shockley partial separations

Comparison of the SFEs determined by TEM and simulations is not straightforward because of their differing underlying definitions and approximations. Experimentally, the Shockley partial separation is assumed to reflect equilibrium between the elastic repulsion of the partials (assuming elastic isotropy) and their attraction to minimize the surface area of the stacking fault. In contrast, extended stacking faults without any dislocations are considered in simulations, *i.e.*, the SFE represents the excess energy per unit area of a stacking fault compared to the perfect lattice. In the simulations, the starting (perfect lattice) and ending energies (stable stacking fault energy) are considered. However, more accurate descriptions should account for the full energy pathway. In this context, Kibey *et al.* [93] suggested that the Shockley partial separation depends on the whole γ-surface (also called GSFE [48]). Using DFT calculations to compute the γ-surface and a generalized Peierls–Nabarro model, Kibey *et al.* [93] pointed out that the unstable SFE (γ_{us} [94]) is a critical parameter governing the separation distance between Shockley partials. As shown in Section G of the supplementary materials, we find that this correction is particularly important for alloys with high SFEs (*i.e.*, with large core effects) while the Volterra solution provided in Eq. S10 is an excellent approximation for low SFEs.

To compute the Shockley partial separation distances, we sampled the γ-surface at six points with the PAW method. The coordinates of these points, the corresponding energies and statistical uncertainties are reported in Table 5. The GSFEs were used to parametrize the γ-surface with Eq. S14. From this, following the Peierls-Nabarro formalism outlined in Section G of the supplementary materials, we computed the Shockley partial separation distances reported in Fig. 9b employing the elastic moduli and lattice parameters measured experimentally. The computed distances are slightly larger (by 3–5 nm) than those measured by TEM because the intrinsic SFEs calculated with the PAW method are lower than the experimental SFEs (*cf.* Fig. 9c). The statistical error bars on the separation distances are very large and are almost entirely determined by the corresponding uncertainties of the intrinsic SFEs. For the $Cr_{26}Mn_{20}Fe_{20}Co_{20}Ni_{14}$ alloy, the lower bound of the error bar is even negative, which would lead to an infinite partial separation distance. However, it is worth noting that these *ab initio* simula-

Table 5
Generalized stacking fault energies in mJ/m^2 computed with the PAW method (VASP) for $Cr_{12.9}Mn_{20.4}Fe_{20.4}Co_{20.4}Ni_{25.9}$ and $Cr_{25.9}Mn_{20.4}Fe_{20.4}Co_{20.4}Ni_{12.9}$ at six disregistry points.

	GSFE (mJ/m^2)	
(u_x, u_z)	$Cr_{14}Mn_{20}Fe_{20}Co_{20}Ni_{26}$	$Cr_{26}Mn_{20}Fe_{20}Co_{20}Ni_{14}$
$(0, \frac{\sqrt{3}}{12}b)$	151 ± 21	183 ± 17
$(0, \frac{\sqrt{3}}{6}b)$ $[\gamma_{usf}]$	282 ± 19	309 ± 20
$(0, \frac{\sqrt{3}}{3}b)$ $[\gamma_{isf}]$	30 ± 24	11 ± 16
$(0, \frac{2\sqrt{3}}{3}b)$ $[\gamma_{max}]$	1455 ± 20	1524 ± 21
$(\frac{1}{4}b, 0)$	449 ± 20	462 ± 24
$(\frac{1}{2}b, 0)$	779 ± 21	769 ± 22

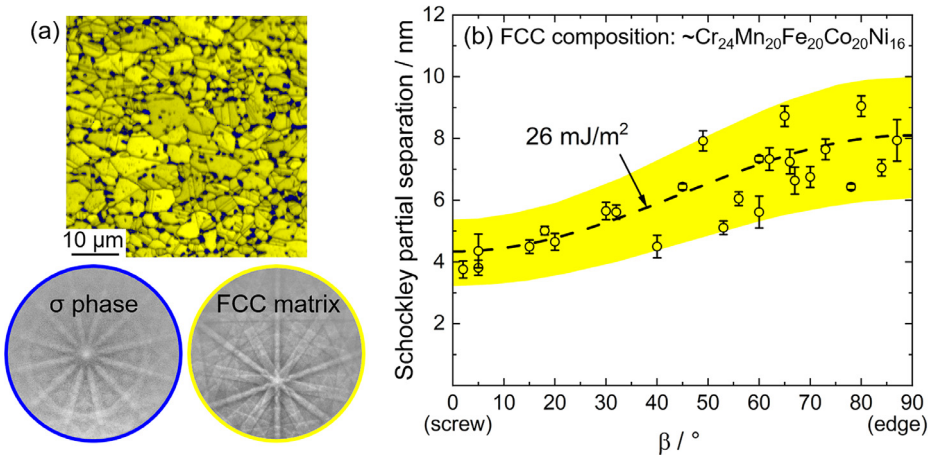

Fig. 10. Microstructure and Shockley partial separation distances in a two-phase σ+FCC $Cr_{26}Mn_{20}Fe_{20}Co_{20}Ni_{14}$ HEA. (a) Phase map obtained by EBSD where the FCC matrix is shown in yellow and the σ precipitates in blue. Two corresponding Kikuchi maps from the σ and FCC phases are shown at the bottom. (b) Shockley partial separation as a function of dislocation character (β) for the FCC matrix with an average composition: $Cr_{24}Mn_{20}Fe_{20}Co_{20}Ni_{16}$.

tions reasonably reproduce the experimental trend despite the fact that the simulations were performed at 0 K in a ferrimagnetic state while the experiments were carried out at 300 K, at which the alloys are paramagnetic.

To further verify the validity of the parameters utilized for fitting the γ-surface, we computed the single-crystal shear modulus using the following expression [95]

$$G_{\{111\}\langle 1\bar{1}0\rangle} = \max_{u_x}\left\{2\pi\frac{\partial\gamma}{\partial u_x}\right\}. \quad (6)$$

We obtained values of 63 ± 2 GPa and 64 ± 3 GPa for the $Cr_{14}Mn_{20}Fe_{20}Co_{20}Ni_{26}$ and $Cr_{26}Mn_{20}Fe_{20}Co_{20}Ni_{14}$ alloys, respectively, *i.e.*, $G_{\{111\}\langle 1\bar{1}0\rangle}$ appears to be almost independent of the Cr/Ni ratio, in excellent agreement with the data shown in Figs. 5a-b. These values are very close to the experimentally estimated $G_{\{111\}\langle 1\bar{1}0\rangle}$ for the Cantor alloy, 56 GPa, using the following expression [96]

$$G_{\{111\}\langle 1\bar{1}0\rangle} = \frac{3(c_{11}-c_{12})c_{44}}{c_{11}-c_{12}+4c_{44}}, \quad (7)$$

and the single-crystal elastic constants reported by Teramoto *et al.* [86] extrapolated to 0 K[2].

5. Discussion

5.1. Effect of precipitation of the σ phase on the SFE

A piece of the cold-worked $Cr_{26}Mn_{20}Fe_{20}Co_{20}Ni_{14}$ HEA was annealed at 1173 K for 1 h. The resulting microstructure is displayed in the EBSD phase map of Fig. 10a where a two-phase σ+FCC microstructure can be observed. Here the FCC matrix and σ particles are shown in yellow and blue, respectively, and two representative Kikuchi patterns from these phases are presented at the bottom of Fig. 10a. From the phase map, the σ-phase surface area percentage was estimated to be ~6%, which is lower than the equilibrium volume fraction of ~18% at 1173 K [31], indicating that this is not an equilibrium state. Due to the precipitation of the Cr-rich σ phase, the FCC matrix is correspondingly depleted and its composition, which was determined by TEM-EDX far away from the precipitates, was found to be approximately $Cr_{24}Mn_{20}Fe_{20}Co_{20}Ni_{16}$ (average of five measurements).

[2] Note that the temperature dependencies of the elastic moduli (E and G) reported by Teramoto *et al.* for isotropic polycrystals are in excellent agreement with those shown in Figs. 5a,b.

Using WBDF imaging, the dissociation width of perfect dislocations was determined in regions far away from σ particles. The results are displayed in Fig. 10b where the partial separations in the two-phase σ+FCC $Cr_{26}Mn_{20}Fe_{20}Co_{20}Ni_{14}$ alloy range from ~4 to 8 nm whereas they are between ~5 and 10 nm when the alloy was annealed at a higher temperature to establish a single-phase FCC microstructure (compare Figs. 10b and 9a). This indicates that the SFE decreases with the precipitation of the σ phase due to a change of the Cr/Ni ratio. As the FCC composition in the two-phase alloy was found to be $Cr_{24}Mn_{20}Fe_{20}Co_{20}Ni_{16}$, the corresponding SFE is marked with an empty symbol in Fig. 9c at a Cr concentration of 24 at.%. Its value (26 mJ/m^2) is consistent with the SFE expected based on a linear interpolation of the filled data points, see Fig. 9c. If we now compare the scatter of the data points in single-phase and two-phase alloys in Figs. 10b and 9a, the experimental dispersion is slightly larger for the two-phase alloy. This is probably due to the composition of the FCC matrix in the two-phase alloy being heterogeneous since the precipitation of the σ phase is incomplete, *i.e.*, there are concentration gradients in the FCC matrix and the Cr/Ni ratio gradually decreases and thus the partial separation decreases as one approaches the σ particles [32]. More importantly, our results demonstrate that the SFE of HEAs can be engineered through the precipitation of a secondary phase.

5.2. Can local-SFE fluctuations in HEAs be detected by weak-beam dark-field imaging?

Several theoretical simulations of MEAs [97] and HEAs [98,99] have indicated there should be variations in the local atomic configuration/chemistry along the dislocation line leading to variations in the local SFEs and, in turn, the distance between Shockley partials. Consistent with this notion, separation distances measured in the CrMnFeCoNi HEA using LAADF/HAADF STEM, Nye tensor and center of symmetry analysis showed large variations at different locations, associated with complex solute configurations [98]. To our knowledge, similar analyses for pure metals are not available for a direct comparison. However, as pointed out in a recent paper [5], Shockley partial spacings in HEAs/MEAs, and in the pure metals Cu and Ag, all determined from WBDF analyses, show a similar spread in dissociation widths suggesting that compositional variations along the dislocation line are not the cause of the observed fluctuations in partial separations, at least when imaged in the WBDF mode. For further clarification, we compare in Fig. 11a,b our data for HEAs with those reported in the literature for pure copper [43] (medium SFE) and silver [43,100] (low SFE). The slopes at the

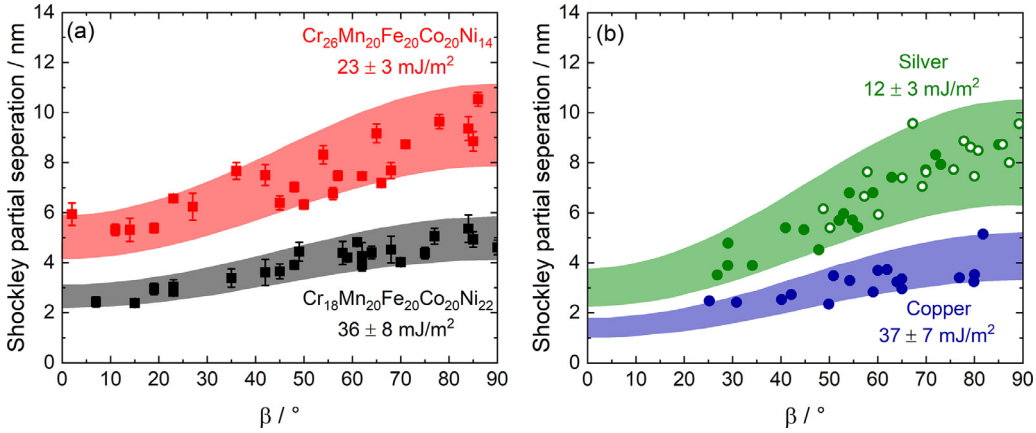

Fig. 11. Stacking fault widths in FCC (a) HEAs and (b) pure metals. The plots show the Shockley partial separation *versus* angle β determined by WBDF imaging. (a) Data obtained in the present study for the $Cr_{14}Mn_{20}Fe_{20}Co_{20}Ni_{26}$ and $Cr_{26}Mn_{20}Fe_{20}Co_{20}Ni_{14}$ HEAs. (b) Data from the literature for Cu [43] and Ag [43,100]. The experimental scatter bands are similar for HEAs and pure metals. Below each alloy designation, the SFEs are noted.

inflection points of the S-shaped curves appear somewhat steeper for the pure metals compared to the HEAs. This is related to the Poisson's ratio of these different classes of materials: 0.37–0.40 for pure Cu and Ag and ~0.26 for our HEAs. However, the experimental scatter bands of the S-shaped curves are similar for the HEAs and pure metals. Since partial separations and, therefore, local variations in SFE are not discernably different in HEAs compared to pure metals, at least when using WBDF images, techniques similar to those in [98] must be applied to pure metals to better quantify the degree of difference (if any) between highly alloyed and dilute/pure metals.

5.3. Systematic offset between experimentally determined and ab initio calculated SFEs

Several computational papers have predicted that the Cantor alloy should have near-zero or even a negative SFE at 0 K [101–107], while experimental values at 293 K range between 28 and 35 mJ/m^2 [5,21,22,24,108]. This discrepancy has triggered a debate on "negative SFEs" [109–113]. In this context, it is important to note that absolute values computed from DFT can be often off for several reasons although compositional trends are usually much better described. A typical example is over-/under-binding related to different approximations of the exchange-correlation functional in DFT resulting in under-/overestimated absolute lattice constants [114], which can have strong effects on SFEs. For instance, for the Cantor alloy, the SFE can be higher if calculations are performed using the experimental lattice constants rather than the significantly smaller computationally predicted ones (Table 3) whereas compositional trends are hardly affected [115].

Besides the systematic errors due to the approximations of DFT, as mentioned here and elsewhere, five additional factors can be responsible for the offset between theoretical and experimental SFEs, namely:

(1) Finite temperature effects
(2) Atomic relaxations
(3) Magnetic effects
(4) Chemical short-range ordering (SRO) [116–119]
(5) Strong dislocation/solute interactions [111] or lattice frictions [88] that counteract the elastic repulsion of the partials

All these explanations are plausible, but their experimental validation/refutation is extremely challenging. Here, we limit our comments to points (1–3) since they were investigated in the present study. By comparing the EMTO data at 0 K and 300 K in Fig. 9c, it is evident that finite temperature effects play an important role in determining the SFE. Moreover, by looking at the PAW data, it can be seen that atomic relaxations have a similar impact. Both contributions increase the SFE substantially, bringing it closer to experimental values. These two factors are clearly not independent from each other and cannot be simply added up, but they may be sufficient to account for the systematic shift between theory and experiments. Therefore, we argue that good quantitative agreement with the experimental data could be reached if it was possible to simultaneously consider all the different ingredients, namely: (i) vibrational, electronic, and magnetic excitations; (ii) atomic relaxations. Unfortunately, computational approaches that account for all these contributions at once are presently too expensive for compositionally complex materials, hence the best compromise must be sought in practice.

6. Conclusions

Ten pseudobinary HEAs, $Cr_xMn_{20}Fe_{20}Co_{20}Ni_{40-x}$, spanning a broad composition range $0 \leq x \leq 26$ at.% were investigated. All the alloys were chemically homogeneous, untextured, and single-phase FCC in the recrystallized state. The physical properties of these alloys, including their lattice parameters, melting range, thermal behavior, elastic moduli, magnetism and stacking fault energies were measured and compared with *ab initio* calculations. From the obtained results, the following conclusions can be drawn:

- The lattice parameter ($a \approx 0.3599$ nm) of all the investigated alloys at 293 K is approximately independent of composition. The solidus temperature increases linearly by ~30 K with increasing x from 0 to 26 at.% while the liquidus temperature is roughly independent of composition.
  - For $x \geq 10$ at.%, the HEAs are not magnetic between 100 and 673 K. Additionally, the temperature dependence of the coefficients of thermal expansion and elastic moduli of these alloys are nearly identical. The average temperature dependencies of the Young's and shear moduli are given by:
  - $E(T) = 214.5 - \frac{21.7}{e^{\frac{271}{T}}-1}$ and $G(T) = 85.4 - \frac{9.7}{e^{\frac{275.3}{T}}-1}$
  - Two of the alloys $Cr_5Mn_{20}Fe_{20}Co_{20}Ni_{35}$ and $Mn_{20}Fe_{20}Co_{20}Ni_{40}$ become magnetic below critical temperatures of ~200 K and ~440 K, respectively. These Curie temperatures are qualitatively reproduced by our *ab initio* calculations. The magnetic transitions are associated with magnetostriction, which is clearly visible on the $\alpha(T)$ and $Q^{-1}(T)$ curves.
  - Experimentally, the SFE at 300 K increases linearly from 23 mJ/m^2 for $Cr_{26}Mn_{20}Fe_{20}Co_{20}Ni_{14}$ to 69 mJ/m^2 for $Cr_{14}Mn_{20}Fe_{20}Co_{20}Ni_{26}$ (the SFE of the equiatomic alloy is

35 mJ/m^2, consistent with previous experimental studies). Theoretical simulations reproduce the compositional trends but the absolute values are systematically lower than the experimental ones.

- Our *ab initio* simulations reveal that atomic relaxations, finite temperature effects, and magnetic effects, when considered individually, have a strong influence on the SFE and if these factors are not accounted for, the SFEs can be greatly underestimated. Therefore, we conjecture that if all these factors were included simultaneously in computations, the experimental and simulation values of the SFEs may match closely. However, such simulations are currently too expensive to perform.
- *Ab initio* calculations were also performed to compute the γ-surface of the $Cr_{26}Mn_{20}Fe_{20}Co_{20}Ni_{14}$ and $Cr_{14}Mn_{20}Fe_{20}Co_{20}Ni_{26}$ HEAs. These calculations in combination with the Peierls-Nabarro formalism allowed us to compute the separation distances between Shockley partials, which were found to reproduce the compositional trend observed experimentally. Additionally, the shear moduli $G_{\{111\}\langle 1\bar{1}0\rangle}$ derived from the γ-surfaces are nearly independent of composition, in agreement with our results, and their magnitudes are consistent with experimental values reported in the literature for the Cantor alloy.

As a final remark, it is worth noting that, in the present work, a broad concentration range ($14 \leq x \leq 26$ at.%) was identified in which the SFE can be finely tuned while all the other physical properties remain almost constant. Therefore, the pseudo-binary subsets of the Cr-MnFeCoNi alloy can be considered as model HEAs to investigate the effect of SFE on mechanical properties without confounding effects of other physical properties.

Declaration of Competing Interest

The authors declare that they have no known competing financial interests or personal relationships that could have appeared to influence the work reported in this paper.

Research data for this article

The research data of the present article can be found on the following Mendeley data repository: https://data.mendeley.com/datasets/8kzkdctdtp/1.

Acknowledgments

GL, FK and GE acknowledge funding from the German Research Foundation (Deutsche Forschungsgemeinschaft DFG) through projects LA 3607/3–2, KO 5080/2–2, and A1/A2 of the SFB/TR 103, respectively. The former two projects are associated with the Priority Program SPP 2006 “Compositionally Complex Alloys - High Entropy Alloys”. AF and FK acknowledge funding from the Nederlandse Organisatie voor Wetenschappelijk Onderzoek (NWO) [VIDI Grant No. 15707]. Part of the calculations were conducted on the Dutch national e-infrastructure with the support of SURF Cooperative. EPG is sponsored by the U.S. Department of Energy, Office of Science, Basic Energy Sciences, Materials Sciences and Engineering Division. The Center for interface-dominated high-performance materials (Zentrum für Grenzflachen-dominierte Höchstleistungswerkstoffe, ZGH) is acknowledged for the use of the Linseis STA PT1600 DSC.

We thank Christopher Bärsch and Philipp Jäschke from the institute of Geology, Mineralogy and Geophysics of the Ruhr-University Bochum for their support in the measurements of coefficients of thermal expansion and elastic constants.

Supplementary materials

Supplementary material associated with this article can be found, in the online version, at doi:10.1016/j.actamat.2022.117693.

References

[1] B. Cantor, I.T.H. Chang, P. Knight, A.J.B. Vincent, Microstructural development in equiatomic multicomponent alloys, Mater. Sci. Eng. A 375 (377) (2004) 213–218, doi:10.1016/j.msea.2003.10.257.
[2] B. Gludovatz, A. Hohenwarter, D. Catoor, E.H. Chang, E.P. George, R.O. Ritchie, A fracture-resistant high-entropy alloy for cryogenic applications, Science 345 (2014) 1153–1158, doi:10.1126/science.1254581.
[3] S. Haas, A.M. Manzoni, F. Krieg, U. Glatzel, Microstructure and Mechanical Properties of Precipitate Strengthened High Entropy Alloy $Al_{10}Co_{25}Cr_8Fe_{15}Ni_{36}Ti_6$ with Additions of Hafnium and Molybdenum, Entropy 21 (2019) 169, doi:10.3390/e21020169.
[4] E.P. George, W.A. Curtin, C.C. Tasan, High entropy alloys: A focused review of mechanical properties and deformation mechanisms, Acta Mater. 188 (2020) 435–474, doi:10.1016/j.actamat.2019.12.015.
[5] M. Kawamura, M. Asakura, N.L. Okamoto, K. Kishida, H. Inui, E.P. George, Plastic deformation of single crystals of the equiatomic Cr−Mn−Fe−Co−Ni high-entropy alloy in tension and compression from 10K to 1273K, Acta Mater. 203 (2021) 116454, doi:10.1016/j.actamat.2020.10.073.
[6] K.Y. Tsai, M.H. Tsai, J.W. Yeh, Sluggish diffusion in Co–Cr–Fe–Mn–Ni high-entropy alloys, Acta Mater. 61 (2013) 4887–4897, doi:10.1016/j.actamat.2013.04.058.
[7] M. Vaidya, K.G. Pradeep, B.S. Murty, G. Wilde, S.V. Divinski, Bulk tracer diffusion in CoCrFeNi and CoCrFeMnNi high entropy alloys, Acta Mater. 146 (2018) 211–224, doi:10.1016/j.actamat.2017.12.052.
[8] G. Laplanche, U.F. Volkert, G. Eggeler, E.P. George, Oxidation Behavior of the CrMnFeCoNi High-Entropy Alloy, Oxid. Met. 85 (2016) 629–645, doi:10.1007/s11085-016-9616-1.
[9] Q. Ye, K. Feng, Z. Li, F. Lu, R. Li, J. Huang, Y. Wu, Microstructure and corrosion properties of CrMnFeCoNi high entropy alloy coating, Appl. Surf. Sci. 396 (2017) 1420–1426, doi:10.1016/j.apsusc.2016.11.176.
[10] Y. Li, A. Kostka, A. Savan, A. Ludwig, Atomic-scale investigation of fast oxidation kinetics of nanocrystalline CrMnFeCoNi thin films, J. Alloys Compd. 766 (2018) 1080–1085, doi:10.1016/j.jallcom.2018.07.048.
[11] C. Stephan-Scherb, W. Schulz, M. Schneider, S. Karafiludis, G. Laplanche, High-Temperature Oxidation in Dry and Humid Atmospheres of the Equiatomic CrMnFeCoNi and CrCoNi High- and Medium-Entropy Alloys, Oxid. Met. 95 (2021) 105–133, doi:10.1007/s11085-020-10014-7.
[12] T. Löffler, A. Savan, A. Garzón-Manjón, M. Meischein, C. Scheu, A. Ludwig, W. Schuhmann, Toward a paradigm shift in electrocatalysis using complex solid solution nanoparticles, ACS Energy Lett. 4 (2019) 1206–1214, doi:10.1021/acsenergylett.9b00531.
[13] A. Gali, E.P. George, Tensile properties of high- and medium-entropy alloys, Intermetallics 39 (2013) 74–78, doi:10.1016/j.intermet.2013.03.018.
[14] F. Otto, A. Dlouhý, C. Somsen, H. Bei, G. Eggeler, E.P. George, The influences of temperature and microstructure on the tensile properties of a CoCrFeMnNi high-entropy alloy, Acta Mater. 61 (2013) 5743–5755, doi:10.1016/j.actamat.2013.06.018.
[15] F. Otto, N.L. Hanold, E.P. George, Microstructural evolution after thermomechanical processing in an equiatomic, single-phase CoCrFeMnNi high-entropy alloy with special focus on twin boundaries, Intermetallics 54 (2014) 39–48, doi:10.1016/j.intermet.2014.05.014.
[16] K. Lu, A. Chauhan, D. Litvinov, M. Walter, A.S. Tirunilai, J. Freudenberger, A. Kauffmann, M. Heilmaier, J. Aktaa, High-temperature low cycle fatigue behavior of an equiatomic CoCrFeMnNi high-entropy alloy, Mater. Sci. Eng. A 791 (2020) 139781, doi:10.1016/j.msea.2020.139781.
[17] K. Lu, A. Chauhan, M. Walter, A.S. Tirunilai, M. Schneider, G. Laplanche, J. Freudenberger, A. Kauffmann, M. Heilmaier, J. Aktaa, Superior low-cycle fatigue properties of CoCrNi compared to CoCrFeMnNi, Scr. Mater. 194 (2021) 113667, doi:10.1016/j.scriptamat.2020.113667.
[18] S. Picak, T. Wegener, S.V. Sajadifar, C. Sobrero, J. Richter, H. Kim, T. Niendorf, I. Karaman, On the low-cycle fatigue response of CoCrNiFeMn high entropy alloy with ultra-fine grain structure, Acta Mater. 205 (2021) 116540, doi:10.1016/j.actamat.2020.116540.
[19] K.V. Thurston, B. Gludovatz, A. Hohenwarter, G. Laplanche, E.P. George, R.O. Ritchie, Effect of temperature on the fatigue-crack growth behavior of the high-entropy alloy CrMnFeCoNi, Intermetallics 88 (2017) 65–72, doi:10.1016/j.intermet.2017.05.009.
[20] K.V.S. Thurston, B. Gludovatz, Q. Yu, G. Laplanche, E.P. George, R.O. Ritchie, Temperature and load-ratio dependent fatigue-crack growth in the CrMnFeCoNi high-entropy alloy, J. Alloys Compd. 794 (2019) 525–533, doi:10.1016/j.jallcom.2019.04.234.
[21] N.L. Okamoto, S. Fujimoto, Y. Kambara, M. Kawamura, Z.M. Chen, H. Matsunoshita, K. Tanaka, H. Inui, E.P. George, Size effect, critical resolved shear stress, stacking fault energy, and solid solution strengthening in the CrMnFeCoNi high-entropy alloy, Sci. Rep. 6 (2016) 35863, doi:10.1038/srep35863.
[22] D. Zhou, Z. Chen, K. Ehara, K. Nitsu, K. Tanaka, H. Inui, Effects of annealing on hardness, yield strength and dislocation structure in single crystals of the equiatomic Cr-Mn-Fe-Co-Ni high entropy alloy, Scr. Mater. 191 (2021) 173–178, doi:10.1016/j.scriptamat.2020.09.039.

[23] G. Laplanche, A. Kostka, O.M. Horst, G. Eggeler, E.P. George, Microstructure evolution and critical stress for twinning in the CrMnFeCoNi high-entropy alloy, Acta Mater. 118 (2016) 152–163, doi:10.1016/j.actamat.2016.07.038.

[24] A.J. Zaddach, C. Niu, C.C. Koch, D.L. Irving, Mechanical Properties and Stacking Fault Energies of NiFeCrCoMn High-Entropy Alloy, J. Minerals, Metals, Mater. Soc. (JOM) 65 (2013) 1780, doi:10.1007/s11837-013-0771-4.

[25] A.J. Zaddach, R.O. Scattergood, C.C. Koch, Tensile properties of low-stacking fault energy high-entropy alloys, Mater. Sci. Eng. A 636 (2015) 373–378, doi:10.1016/j.msea.2015.03.109.

[26] K. Ming, X. Bi, J. Wang, Microstructures and deformation mechanisms of $Cr_{26}Mn_{20}Fe_{20}Co_{20}Ni_{14}$ alloys, Mater. Charact. 134 (2017) 194–201, doi:10.1016/j.matchar.2017.10.022.

[27] J. Moon, Y. Qi, E. Tabachnikova, Y. Estrin, W.-M. Choi, S.-H. Joo, B.-J. Lee, A. Podolskiy, M. Tikhonovsky, H.S. Kim, Deformation-induced phase transformation of $Co_{20}Cr_{26}Fe_{20}Mn_{20}Ni_{14}$ high-entropy alloy during high-pressure torsion at 77K, Mater. Lett. 202 (2017) 86–88, doi:10.1016/j.matlet.2017.05.065.

[28] A. Levenets, I. Kolodiy, N. Berezhnaya, Y. Lipovskaya, Influence of Composition and Microstructure on the Features of Mechanical Properties of Co-Cr-Fe-Mn-Ni High Entropy Alloys, East Eur. J. Phys. 4 (1) (2017) 70–74, doi:10.26565/2312-4334-2017-1-06.

[29] K.A. Christofidou, T.P. McAuliffe, P.M. Mignanelli, H.J. Stone, N.G. Jones, On the prediction and the formation of the sigma phase in $CrMnCoFeNi_x$ high entropy alloys, J. Alloys Compd. 770 (2019) 285–293, doi:10.1016/j.jallcom.2018.08.032.

[30] J. Zhang, G.M. Muralikrishna, A. Asabre, Y. Kalchev, J. Müller, B. Butz, S. Hilke, H. Rösner, G. Laplanche, S.V. Divinski, G. Wilde, Tracer diffusion in the σ phase of the CoCrFeMnNi system, Acta Mater. 203 (2021) 116498, doi:10.1016/j.actamat.2020.116498.

[31] G. Laplanche, S. Berglund, C. Reinhart, A. Kostka, F. Fox, E.P. George, Phase stability and kinetics of σ-phase precipitation in CrMnFeCoNi high-entropy alloys, Acta Mater. 161 (2018) 338–351, doi:10.1016/j.actamat.2018.09.040.

[32] G. Laplanche, Growth kinetics of σ-phase precipitates and underlying diffusion processes in CrMnFeCoNi high-entropy alloys, Acta Mater. 199 (2020) 193–208, doi:10.1016/j.actamat.2020.08.023.

[33] M. Schneider, F. Werner, D. Langenkämper, C. Reinhart, G. Laplanche, Effect of Temperature and Texture on Hall–Petch Strengthening by Grain and Annealing Twin Boundaries in the MnFeNi Medium-Entropy Alloy, Metals 9 (84) (2019), doi:10.3390/met9010084.

[34] M. Schneider, E.P. George, T.J. Manescau, T. Záležák, J. Hunfeld, A. Dlouhý, G. Eggeler, G. Laplanche, Analysis of strengthening due to grain boundaries and annealing twin boundaries in the CrCoNi medium-entropy alloy, Int. J. Plast. 124 (2020) 155–169, doi:10.1016/j.ijplas.2019.08.009.

[35] G. Laplanche, O. Horst, F. Otto, G. Eggeler, E.P. George, Microstructural evolution of a CoCrFeMnNi high-entropy alloy after swaging and annealing, J. Alloys Compd. 647 (2015) 548–557, doi:10.1016/j.jallcom.2015.05.129.

[36] ASTM E112-13Standard Test Methods For Determining Average Grain Size, ASTM International, 2013 West Conshohocken, PA, USAhttps://www.astm.org/Standards/E112.htm.

[37] A. Migliori, J. Sarrao, Resonant Ultrasound Spectroscopy : Applications to Physics, Materials Measurements, and Nondestructive Evaluation, John Wiley & Sons, New York, 1997.

[38] G. Laplanche, M. Schneider, F. Scholz, J. Frenzel, G. Eggeler, J. Schreuer, Processing of a single-crystalline CrCoNi medium-entropy alloy and evolution of its thermal expansion and elastic stiffness coefficients with temperature, Scr. Mater. 177 (2020) 44–48, doi:10.1016/j.scriptamat.2019.09.020.

[39] Y.P. Varshni, Temperature dependence of the elastic constants, Phys. Rev. B 2 (1970) 3952–3958, doi:10.1103/PhysRevB.2.3952.

[40] G. Laplanche, P. Gadaud, C. Bärsch, K. Demtröder, C. Reinhart, J. Schreuer, E.P. George, Elastic moduli and thermal expansion coefficients of medium-entropy subsystems of the CrMnFeCoNi high-entropy alloy, J. Alloys Compd. 746 (2018) 244–255, doi:10.1016/j.jallcom.2018.02.251.

[41] A. Durand, L. Peng, G. Laplanche, J.R. Morris, E.P. George, G. Eggeler, Interdiffusion in Cr–Fe–Co–Ni medium-entropy alloys, Intermetallics 122 (2020) 106789, doi:10.1016/j.intermet.2020.106789.

[42] P.M. Anderson, J.P. Hirth, J. Lothe, Theory of Dislocations, Cambridge university Press, 2017 third ed..

[43] D.J.H. Cockayne, M.L. Jenkins, I.L.F. Ray, The measurement of stacking-fault energies of pure face-centred cubic metals, Philos. Mag. 24 (1971) 1383–1392, doi:10.1080/14786437108217419.

[44] D.J.H. Cockayne, A Theoretical Analysis of the Weak-beam Method of Electron Microscopy, Z. für Naturforschung 27a (1972) 452, doi:10.1515/zna-1972-0313.

[45] D.B. Williams, C.B. Carter, Transmission Electron Microscopy: A Textbook For Materials Science, Springer US, Boston, MA, 1996.

[46] D.T. Pierce, J.A. Jiménez, J. Bentley, D. Raabe, C. Oskay, J.E. Wittig, The influence of manganese content on the stacking fault and austenite/ε-martensite interfacial energies in Fe–Mn–(Al–Si) steels investigated by experiment and theory, Acta Mater. 68 (2014) 238–253, doi:10.1016/j.actamat.2014.01.001.

[47] M.H. Loretto, R.E. Smallman, Defect Analysis in Electron Microscopy, Chapman and Hall, 1975.

[48] V. Vitek, Intrinsic stacking faults in body-centred cubic crystals, Philos. Mag. 18 (1968) 773–786, doi:10.1080/14786436808227500.

[49] L. Vitos, H.L. Skriver, B. Johansson, J. Kollár, Application of the exact muffin-tin orbitals theory: the spherical cell approximation, Comput. Mater. Sci. 18 (2000) 24–38, doi:10.1016/S0927-0256(99)00098-1.

[50] L. Vitos, I.A. Abrikosov, B. Johansson, Anisotropic Lattice Distortions in Random Alloys from First-Principles Theory, Phys. Rev. Lett. 87 (2001) 156401, doi:10.1103/PhysRevLett.87.156401.

[51] A.V. Ruban, H.L. Skriver, Screened Coulomb interactions in metallic alloys. I. Universal screening in the atomic-sphere approximation, Phys. Rev. B 66 (2002) 024201, doi:10.1103/PhysRevB.66.024201.

[52] A.V. Ruban, S.I. Simak, P.A. Korzhavyi, H.L. Skriver, Screened Coulomb interactions in metallic alloys. II. Screening beyond the single-site and atomic-sphere approximations, Phys. Rev. B 66 (2002) 024202, doi:10.1103/PhysRevB.66.024202.

[53] L. Vitos, Computational quantum mechanics for materials engineers: the EMTO method and applications, Springer-Verlag, London, 2007.

[54] L. Vitos, J. Kollár, H.L. Skriver, Full charge-density calculation of the surface energy of metals, Phys. Rev. B 49 (1994) 16694–16701, doi:10.1103/PhysRevB.49.16694.

[55] L. Vitos, J. Kollár, H.L. Skriver, Full charge-density scheme with a kinetic-energy correction: Application to ground-state properties of the 4d metals, Phys. Rev. B 55 (1997) 13521–13527, doi:10.1103/PhysRevB.55.13521.

[56] P.E. Blöchl, Projector augmented-wave method, Phys. Rev. B 50 (1994) 17953, doi:10.1103/PhysRevB.50.17953.

[57] G. Kresse, D. Joubert, From ultrasoft pseudopotentials to the projector augmented-wave method, Phys. Rev. B 59 (1999) 1758, doi:10.1103/PhysRevB.59.1758.

[58] G. Kresse, J. Hafner, Ab initio molecular dynamics for liquid metals, Phys. Rev. B 47 (1993) 558, doi:10.1103/PhysRevB.47.558.

[59] G. Kresse, J. Furthmüller, Efficiency of ab-initio total energy calculations for metals and semiconductors using a plane-wave basis set, Comput. Mater. Sci. 6 (1996) 15–50, doi:10.1016/0927-0256(96)00008-0.

[60] G. Kresse, J. Furthmüller, Efficient iterative schemes for ab initio total-energy calculations using a plane-wave basis set, Phys. Rev. B 54 (1996) 11169, doi:10.1103/PhysRevB.54.11169.

[61] J.P. Perdew, K. Burke, M. Ernzerhof, Generalized gradient approximation made simple, Phys. Rev. Lett. 77 (1996) 3865–3868, doi:10.1103/PhysRevLett.77.3865.

[62] P. Soven, Coherent-Potential model of substitutional disordered alloys, Phys. Rev. 156 (1967) 809–813, doi:10.1103/PhysRev.156.809.

[63] B.L. Gyorffy, Coherent-Potential approximation for a nonoverlapping-muffin-tin-potential model of random substitutional alloys, Phys. Rev. B 5 (1972) 2382–2384, doi:10.1103/PhysRevB.5.2382.

[64] P. Vinet, J.R. Smith, J. Ferrante, J.H. Rose, Temperature effects on the universal equation of state of solids, Phys. Rev. B 35 (1987) 1945–1953, doi:10.1103/PhysRevB.35.1945.

[65] A.O. de-la-Roza, V. Luaña, Gibbs2: a new version of the quasi-harmonic model code. I. Robust treatment of the static data, Comput. Phys. Commun. 182 (2011) 1708–1720, doi:10.1016/j.cpc.2011.04.016.

[66] D. Ma, B. Grabowski, F. Körmann, J. Neugebauer, D. Raabe, Ab initio thermodynamics of the CoCrFeMnNi high entropy alloy: Importance of entropy contributions beyond the configurational one, Acta Mater. 100 (2015) 90–97, doi:10.1016/j.actamat.2015.08.050.

[67] O. Schneeweiss, M. Friák, M. Dudová, D. Holec, M. Šob, D. Kriegner, V. Holý, P. Beran, E.P. George, J. Neugebauer, A. Dlouhý, Magnetic properties of the CrMnFeCoNi high-entropy alloy, Phys. Rev. B 96 (2017) 014437, doi:10.1103/PhysRevB.96.014437.

[68] Z. Rao, B. Dutta, F. Körmann, D. Ponge, L. Li, J. He, L. Stephenson, L. Schäfer, K. Skokov, O. Gutfleisch, D. Raabe, Z. Li, Unveiling the mechanism of abnormal magnetic behavior of FeNiCoMnCu high-entropy alloys through a joint experimental-theoretical study, Phys. Rev. Materials 4 (2020) 014402, doi:10.1103/physrevmaterials.4.014402.

[69] J. Staunton, B.L. Gyorffy, A.J. Pindor, G.M. Stocks, H. Winter, The "disordered local moment" picture of itinerant magnetism at finite temperatures, J. Magn. Magn. Mater. 45 (1984) 15–22, doi:10.1016/0304-8853(84)90367-6.

[70] B.L. Gyorffy, A.J. Pindor, J. Staunton, G.M. Stocks, H. Winter, A first-principles theory of ferromagnetic phase transitions in metals, J. Phys. F Met. Phys. 15 (1985) 1337–1386, doi:10.1088/0305-4608/15/6/018.

[71] P.J.H. Denteneer, W. van Haeringen, Stacking-fault energies in semiconductors from first-principles calculations, J. Phys. C Solid State Phys. 20 (1987) L883, doi:10.1088/0022-3719/20/32/001.

[72] V.L. Moruzzi, J.F. Janak, K. Schwarz, Calculated thermal properties of metals, Phys. Rev. B 37 (1988) 790–799, doi:10.1103/PhysRevB.37.790.

[73] A. Ferrari, Y. Lysogorskiy, R. Drautz, Design of refractory compositionally complex alloys with optimal mechanical properties, Phys. Rev. Materials 5 (2021) 063606, doi:10.1103/PhysRevMaterials.5.063606.

[74] D. Gambino, M.A. Brännvall, A. Ehn, Y. Hedström, B. Alling, Longitudinal spin fluctuations in bcc and liquid Fe at high temperature and pressure calculated with a supercell approach, Phys. Rev. B 102 (2020) 014402, doi:10.1103/PhysRevB.102.014402.

[75] I. Bleskov, T. Hickel, J. Neugebauer, A. Ruban, Impact of local magnetism on stacking fault energies: a first-principles investigation for fcc iron, Phys. Rev. B 93 (2016) 214115, doi:10.1103/PhysRevB.93.214115.

[76] M.P.A.T. Methfessel, A.T. Paxton, High-precision sampling for Brillouin-zone integration in metals, Phys. Rev. B 40 (1989) 3616, doi:10.1103/PhysRevB.40.3616.

[77] X. Liu, Z. Pei, M. Eisenbach, Dislocation core structures and Peierls stresses of the high-entropy alloy NiCoFeCrMn and its subsystems, Mater. Des. 180 (2019) 107955, doi:10.1016/j.matdes.2019.107955.

[78] R. Peierls, The size of a dislocation, in: Proceedings of the Physical Society. Section A, 52, Proc. Phys. Soc, Section A 52, 1940, pp. 34–37. https://iopscience.iop.org/article/10.1088/0959-5309/52/1/305/meta?casa_token=OnWn6wMtw9kAAAAA:OUVgOE-eHtcMOiSkwNRDiCyLqIWaHJ7IFE95_EoFzY7nooKTTOcJckn5Q1oqb3OpWgubWvssesI.

[79] F.R.N. Nabarro, Dislocations in a simple cubic lattice, in: Proceedings of the Physical Society. Section A, 59, Proc. Phys. Soc, Section A 59, 1947, pp. 256–272. https://iopscience.iop.org/article/10.1088/0959-5309/59/2/309/meta?casa_token=szxZez2YspsAAAAA:jIoakPh7Eqnyvg1Rp96rFL82R6oxjtQ6ObG8ZEmAyMWfELhhUZu-ADkek5j_nvVuzx7-KUImcYA.

[80] D. Rodney, J. Bonneville, Dislocations, in: D. Laughlin, K. Hono (Eds.), Physical Metallurgy, Elsevier, 2014, pp. 1591–1680.

[81] L. Lutterotti, S. Matthies, H. Wenk, MAUD: a friendly Java program for material analysis using diffraction, IUCr: Newsletter of the CPD 21 (1999).

[82] P.P. Bhattacharjee, G.D. Sathiaraj, M. Zaid, J.R. Gatti, C. Lee, C.-W. Tsai, J.-W. Yeh, Microstructure and texture evolution during annealing of equiatomic CoCrFeMnNi high-entropy alloy, J. Alloys Compd. 587 (2014) 544–552, doi:10.1016/j.jallcom.2013.10.237.

[83] M. Laurent-Brocq, A. Akhatova, L. Perrière, S. Chebini, X. Sauvage, E. Leroy, Y. Champion, Insights into the phase diagram of the CrMnFeCoNi high entropy alloy, Acta Mater. 88 (2015) 355–365, doi:10.1016/j.actamat.2015.01.068.

[84] G. Laplanche, P. Gadaud, O. Horst, F. Otto, G. Eggeler, E.P. George, Temperature dependencies of the elastic moduli and thermal expansion coefficient of an equiatomic, single-phase CoCrFeMnNi high-entropy alloy, J. Alloys Compd. 623 (2015) 348–353, doi:10.1016/j.jallcom.2014.11.061.

[85] A. Haglund, M. Koehler, D. Catoor, E.P. George, V. Keppens, Polycrystalline elastic moduli of a high-entropy alloy at cryogenic temperatures, Intermetallics 58 (2015) 62–64, doi:10.1016/j.intermet.2014.11.005.

[86] T. Teramoto, K. Yamada, R. Ito, K. Tanaka, Monocrystalline elastic constants and their temperature dependences for equi-atomic Cr-Mn-Fe-Co-Ni high-entropy alloy with the face-centered cubic structure, J. Alloys Compd. 777 (2019) 1313–1318, doi:10.1016/j.jallcom.2018.11.052.

[87] G. Laplanche, P. Gadaud, L. Perrière, I. Guillot, J.P. Couzinié, Temperature dependence of elastic moduli in a refractory HfNbTaTiZr high-entropy alloy, J. Alloys Compd. 799 (2019) 538–545, doi:10.1016/j.jallcom.2019.05.322.

[88] Y.X. Ye, B.L. Musico, Z.Z. Lu, L.B. Xu, Z.F. Lei, V. Keppens, H.X. Xu, T.G. Nieh, Evaluating elastic properties of a body-centered cubic NbHfZrTi high-entropy alloy – a direct comparison between experiments and ab initio calculations, Intermetallics 109 (2019) 167–173, doi:10.1016/j.intermet.2019.04.003.

[89] F. Körmann, D. Ma, D.D. Belyea, M.S. Lucas, C.W. Miller, B. Grabowski, M.H.F. Sluiter, Treasure maps" for magnetic high-entropy-alloys from theory and experiment, Appl. Phys. Lett. 107 (2015) 142404, doi:10.1063/1.4932571.

[90] A.V. Ruban, S. Khmelevskyi, P. Mohn, B. Johansson, Temperature-induced longitudinal spin fluctuations in Fe and Ni, Phys. Rev. B 75 (2007) 054402, doi:10.1103/PhysRevB.75.054402.

[91] S. Khmelevskyi, P. Mohn, Magnetostriction in Fe-based alloys and the origin of the Invar anomaly, Phys. Rev. B 69 (2004) 140404, doi:10.1103/PhysRevB.69.140404.

[92] Z. Rao, D. Ponge, F. Körmann, Y. Ikeda, O. Schneeweiss, M. Friák, J. Neugebauer, D. Raabe, Z. Li, Invar effects in FeNiCo medium entropy alloys: From an Invar treasure map to alloy design, Intermetallics 111 (2019) 106520, doi:10.1016/j.intermet.2019.106520.

[93] S. Kibey, J.B. Liu, M.J. Curtis, D.D. Johnson, H. Sehitoglu, Effect of nitrogen on generalized stacking fault energy and stacking fault widths in high nitrogen steels, Acta Mater. 54 (2006) 2991–3001, doi:10.1016/j.actamat.2006.02.048.

[94] J.R. Rice, Dislocation nucleation from a crack tip: An analysis based on the Peierls concept, J. Mech. Phys. Solids 40 (1992) 239–271, doi:10.1016/S0022-5096(05)80012-2.

[95] L. Patriarca, A. Ojha, H. Sehitoglu, Y.I. Chumlyakov, Slip nucleation in single crystal FeNiCoCrMn high entropy alloy, Scr. Mater. 112 (2016) 54–57, doi:10.1016/j.scriptamat.2015.09.009.

[96] D. Siebörger, H. Knake, U. Glatzel, Temperature dependence of the elastic moduli of the nickel-base superalloy CMSX-4 and its isolated phases, Mater. Sci. Eng. A 298 (2001) 26–33, doi:10.1016/S0921-5093(00)01318-6.

[97] Q.-J. Li, H. Sheng, E. Ma, Strengthening in multi-principal element alloys with local-chemical-order roughened dislocation pathways, Nat. Commun. 10 (2019) 3563, doi:10.1038/s41467-019-11464-7.

[98] T.M. Smith, M.S. Hooshmand, B.D. Esser, F. Otto, D.W. McComb, E.P. George, M. Ghazisaeidi, M.J. Mills, Atomic-scale characterization and modeling of 60° dislocations in a high-entropy alloy, Acta Mater. 110 (2016) 352–363, doi:10.1016/j.actamat.2016.03.045.

[99] Y. Ikeda, F. Körmann, I. Tanaka, J. Neugebauer, Impact of chemical fluctuations on stacking fault energies of CrCoNi and CrMnFeCoNi high entropy alloys from first principles, Entropy 20 (2018), doi:10.3390/e20090655.

[100] H. Saka, T. Iwata, T. Imura, Temperature dependence of the stacking-fault energy in pure silver, Philos. Mag. A 37 (1978) 291–296, doi:10.1080/01418617808235441.

[101] S. Huang, W. Li, S. Lu, F. Tian, J. Shen, E. Holmström, L. Vitos, Temperature dependent stacking fault energy of FeCrCoNiMn high entropy alloy, Scr. Mater. 108 (2015) 44–47, doi:10.1016/j.scriptamat.2015.05.041.

[102] S. Zhao, G.M. Stocks, Y. Zhang, Stacking fault energies of face-centered cubic concentrated solid solution alloys, Acta Mater. 134 (2017) 334–345, doi:10.1016/j.actamat.2017.05.001.

[103] H. Huang, X. Li, Z. Dong, W. Li, S. Huang, D. Meng, X. Lai, T. Liu, S. Zhu, L. Vitos, Critical stress for twinning nucleation in CrCoNi-based medium and high entropy alloys, Acta Mater. 149 (2018) 388–396, doi:10.1016/j.actamat.2018.02.037.

[104] S. Huang, H. Huang, W. Li, D. Kim, S. Lu, X. Li, E. Holmström, S.K. Kwon, L. Vitos, Twinning in metastable high-entropy alloys, Nat. Commun. 9 (2018) 2381, doi:10.1038/s41467-018-04780-x.

[105] C. Niu, C.R. LaRosa, J. Miao, M.J. Mills, M. Ghazisaeidi, Magnetically-driven phase transformation strengthening in high entropy alloys, Nat. Commun. 9 (2018) 1363, doi:10.1038/s41467-018-03846-0.

[106] Z. Dong, S. Schönecker, W. Li, D. Chen, L. Vitos, Thermal spin fluctuations in CoCrFeMnNi high entropy alloy, Sci. Rep. 8 (2018) 12211, doi:10.1038/s41598-018-30732-y.

[107] Y. Ikeda, I. Tanaka, J. Neugebauer, F. Körmann, Impact of interstitial C alloying on phase stability and stacking fault energy of the CrMnFeCoNi high-entropy alloy, Phys. Rev. Materials 3 (2019) 113603, doi:10.1103/PhysRevMaterials.3.113603.

[108] S.F. Liu, Y. Wu, H.T. Wang, J.Y. He, J.B. Liu, C.X. Chen, X.J. Liu, H. Wang, Z.P. Lu, Stacking fault energy of face-centered-cubic high entropy alloys, Intermetallics 93 (2018) 269–273, doi:10.1016/j.intermet.2017.10.004.

[109] X. Sun, S. Lu, R. Xie, X. An, W. Li, T. Zhang, C. Liang, X. Ding, Y. Wang, H. Zhang, L. Vitos, Can experiment determine the stacking fault energy of metastable alloys? Mater. Des. 199 (2021) 109396, doi:10.1016/j.matdes.2020.109396.

[110] Z. Pei, B. Dutta, F. Körmann, M. Chen, Hidden Effects of Negative Stacking Fault Energies in Complex Concentrated Alloys, Phys. Rev. Lett. 126 (2021) 255502, doi:10.1103/PhysRevLett.126.255502.

[111] M. Shih, J. Miao, M. Mills, M. Ghazisaeidi, Stacking fault energy in concentrated alloys, Nat. Commun. 12 (2021) 1–10, doi:10.1038/s41467-021-23860-z.

[112] B. Yin, S. Yoshida, N. Tsuji, W.A. Curtin, Yield strength and misfit volumes of NiCoCr and implications for short-range-order, Nat. Commun. 11 (2020) 1–7, doi:10.1038/s41467-020-16083-1.

[113] R. Zhang, S. Zhao, J. Ding, Y. Chong, T. Jia, C. Ophus, M. Asta, R.O. Ritchie, A.M. Minor, Short-range order and its impact on the CrCoNi medium-entropy alloy, Nature 581 (2020) 283–287, doi:10.1038/s41586-020-2275-z.

[114] B. Grabowski, T. Hickel, J. Neugebauer, Ab initio study of the thermodynamic properties of nonmagnetic elementary fcc metals: Exchange-correlation-related error bars and chemical trends, Phys. Rev. B 76 (2007) 024309, doi:10.1103/PhysRevB.76.024309.

[115] Z. Li, F. Körmann, B. Grabowski, J. Neugebauer, D. Raabe, Ab initio assisted design of quinary dual-phase high-entropy alloys with transformation-induced plasticity, Acta Mater. 136 (2017) 262–270, doi:10.1016/j.actamat.2017.07.023.

[116] Y. Ikeda, F. Körmann, I. Tanaka, J. Neugebauer, Impact of Chemical Fluctuations on Stacking Fault Energies of CrCoNi and CrMnFeCoNi High Entropy Alloys from First Principles, Entropy 20 (2018) 655, doi:10.3390/e20090655.

[117] S. Zhao, Y. Osetsky, G.M. Stocks, Y. Zhang, Local-environment dependence of stacking fault energies in concentrated solid-solution alloys, npj, Comput. Mater. 5 (2019) 13, doi:10.1038/s41524-019-0150-y.

[118] Q. Ding, H. Bei, X. Wei, Y.F. Gao, Z. Zhang, Nano-twin-induced exceptionally superior cryogenic mechanical properties of a Ni-based GH3536 (Hastelloy X) superalloy, Mater. Today Nano 14 (2021) 100110, doi:10.1016/j.mtnano.2021.100110.

[119] F. Walsh, M. Asta, R.O. Ritchie, Magnetically driven short-range order can explain anomalous measurements in CrCoNi, in: Proceedings of the National Academy of Sciences of the United States of America, 118, PNAS America, 2021, doi:10.1073/pnas.2020540118.